Comparison of Planar Dipoles in UWB Applications

Xuan Hui Wu[1,2], *Student Member, IEEE*, Zhi Ning Chen[1], *Member, IEEE*

[1]Department of Radio Systems, Institute for Infocomm Research
20 Science Park Road, #02-21/25 TeleTech Park, Singapore 117674

[2]Department of Electrical and Computer Engineering
National University of Singapore
10 Kent Ridge Crescent, Singapore 119260
E-mail: xuanhui_wu@ieee.org, chenzn@i2r.a-star.edu.sg

Abstract

The characteristics of four planar dipoles are studied and compared based on the design considerations of UWB antennas. Their impedance matching, realized gain, and polarization over the UWB band are investigated. The current distributions on the dipoles are illustrated to interpret their different radiation characteristics. Furthermore, pulses radiated in different directions are presented for both single-band and multi-band schemes in UWB applications.

1 Introduction

In ultra-wide band (UWB) radio applications, the impedance and radiation performances of an antenna such as impedance matching, gain, and polarization are desirable to keep stable over the UWB band of 3.1-10.6 GHz [1, 2]. In addition, the gain and polarization over the UWB band are expected to be independent of the directions of interest. These strict requirements make the design of UWB antennas a great challenge. Planar antennas are suitable for wide band applications due to their broad impedance bandwidths and compact size [3, 4, 5], and the impedance bandwidths can be further widened by using some techniques [6, 7]. Recently, some planar antennas have been proposed for UWB applications. For example, the planar square monopole, disc/half-disc antenna, bottom fed elliptical antenna, stepped-fat dipole antenna, and diamond dipole antenna were studied for UWB systems [8, 9, 10, 11, 12].

This Paper studies the characteristics of four broadband planar dipoles in accordance to the design considerations of UWB antennas. One is a center-fed planar square dipole proposed in [4], and the other three are derived from that one by offsetting the feed point [7], beveling the plate, or introducing a shorting pin. The last two techniques were used together in [6] to improve the impedance bandwidth. The dipoles are analyzed and compared in both frequency and time domains. In the frequency-domain, they are evaluated in terms of impedance matching, realized gain, and polarization over the UWB band. Particularly, the current distributions on the dipoles are investigated in order to interpret their different radiation characteristics. In the time-domain, the waveforms of pulses radiated in different directions are examined.

This Paper is organized as follows. In the next section, the geometries of the dipoles are illustrated, and the return loss as well as realized gain measured to verify the simulated results. Next, the impedance characteristics over the UWB band are compared. Then, the realized gain and polarization are investigated. After that, the current distributions at three operating frequencies are illustrated to interpret the resulting radiation performances. Lastly, the time-domain radiated pulses are presented for both the single-band and multi-band schemes.

2 Comparison of simulated & measured results

Four planar dipoles and the coordinate system are shown in Figure 1, where the dipoles are placed in the x-z plane, each excited by a voltage source with a 100Ω internal resistance. The selection of 100Ω is for the convenience of comparing the simulated results to measurement where equivalent monopoles of the dipoles are excited by 50Ω coaxial probes. The details of the dipoles are given below.

- Ant. A: a center-fed square dipole
- Ant. B: a beveled center-fed square dipole
- Ant. C: an offset-fed square dipole
- Ant. D: a center-fed square dipole with a shorting pin

The simulation is carried out by an EM software package (XFDTD) based on an FDTD method, and the measurement by a Vector Network Analyzer E8364B to verify the simulated results. The simulated and measured $|S_{11}(\omega)|$ as well as realized gain ($G_{real}(\omega)$) in $\theta = \phi = 90^\circ$ direction are plotted in Figure 3 for all the dipoles. The $G_{real}(\omega)$ in the simulation is obtained from (1), where

$G_{abs}(\omega)$ is the absolute gain. However, in the measurement, (1) cannot be used directly because it is not easy to measure the $G_{abs}(\omega)$ over the entire UWB band. Instead, the Friis transmission formula in (2) is used to calculate the $G_{real}(\omega)$. In a transmitting/receiving antenna pair where two identical dipoles are face-to-face located, $G_{abs1}(\omega) = G_{abs2}(\omega)$, $S_{11}(\omega) = S_{22}(\omega)$, $e_1 = e_2 = 100\%$, $|\hat{\rho}_1 \cdot \hat{\rho}_2| = 1$, and $R_{load} = R_s$ are assumed, thus leading to (3). Therefore, after obtaining the measured $|S_{21}(\omega)|$ of the antenna pair, the measured $G_{real}(\omega)$ of the dipole can be calculated. For measurement convenience, the $|S_{21}(\omega)|$ is not measured for a pair of dipoles, but for a pair of equivelent monopoles based on image theorm, Figure 2 shows the measurement set-up for Ant. A, where a pair of identical monopoles are face-to-face mounted on a 755×310-mm ground plane, and separated by a distance of 655mm. Each monopole is connected to a 50Ω coaxial cable through a probe of radius 0.6 mm. For the other three antennas, the measurement set-up is the same except for replacing the two square plates with the correspondence equivalent monopoles of Ants. B, C, and D. In Figure 3, compared to the simulated results of all the dipoles, the lower gain observed in the measured results after 8 GHz may be due to the ohmic loss which is not considered in the calculation.

$$G_{real}(\omega) = G_{abs}(\omega)(1 - |S_{11}(\omega)|^2) \tag{1}$$

$$\begin{aligned} |S_{21}(\omega)|^2 &= \frac{P_r R_{load}}{P_t R_s} \\ &= G_{abs1}(\omega) G_{abs2}(\omega)(1 - |S_{11}(\omega)|^2)(1 - |S_{22}(\omega)|^2)(\frac{\lambda}{4\pi r})^2 e_1 e_2 |\hat{\rho}_1 \cdot \hat{\rho}_2| \frac{R_{load}}{R_s} \\ e_{1,2}: &\quad \text{Antenna efficiency} \\ |\hat{\rho}_1 \cdot \hat{\rho}_2|: &\quad \text{Polarization matching factor} \\ R_s: &\quad \text{Internal resistance of the voltage source} \\ R_{load}: &\quad \text{Load of the receiving antenna} \\ r: &\quad \text{Distance between the transmitting and receiving antennas} \end{aligned} \tag{2}$$

$$G_{real}(\omega) = |S_{21}(\omega)| \frac{4\pi r}{\lambda} \tag{3}$$

3 Impedance characteristics

The simulated impedance bandwidth for $|S_{11}(\omega)| < -10$dB is tabulated in Table 1. It can be seen that Ant. C has the broadest impedance bandwidth, and Ant. A the narrowest. The simulated and measured input impedance responses are illustrated in Figure 4, where the measured results obtained from the equivalent monopoles are multiplied by 2 in order to compare with the simulated results. Three observations can be made from Figure 4. Firstly, Ant. C features the most stable impedance response, with the real and imaginary parts around 100Ω and 0Ω, respectively, thus resulting in

the broadest impedance bandwidth. Secondly, the shorting pin of Ant. D introduces an additional resonance at around 2.7 GHz. Lastly, at operating frequencies below 2.7 GHz, the impedance of Ants. A-C are capacitive while that of Ant. D is inductive due to the shorting pin.

4 Radiation characteristics: polarization & $G_{real}(\omega)$

The far-field radiation characteristics including polarization and $G_{real}(\omega)$ in *x-y* and *y-z* planes are investigated numerically, and plotted in Figures 5 and 6, respectively.

In the *x-y* plane, all the dipoles are linearly polarized in the *z*-direction because of their symmetrical geometries about the *x-y* plane. From Figure 5, the $G_{real}(\omega)$ in different directions may vary so greatly that it is stable over the UWB band in some directions but unstable in the other directions. To investigate the variation of $G_{real}(\omega)$ with the radiation direction, the maximum difference (ΔG_{max}) of the $G_{real}(\omega)$ over the UWB band is calculated in (4). The ΔG_{max} and the corresponding frequency are tabulated in Table 2 for $|\phi| \leq 60°$, and Table 3 for $60° \leq |\phi| \leq 180°$. The results show that in contrast to Ant. A, the $G_{real}(\omega)$ of Ants. B-D are more stable with different radiation directions when $|\phi| \leq 60°$. However, for $60° \leq |\phi| \leq 180°$, the $G_{real}(\omega)$ of Ant. A changes the least.

$$\Delta G_{max} = \text{MAX}\{|G_{real}(f, \theta_1, \phi_1) - G_{real}(f, \theta_2, \phi_2)|\} \quad (4)$$

where 3.1 GHz $\leq f \leq$ 10.6 GHz and $\theta_1 = \theta_2 = 90°$.

In the *y-z* plane, the $G_{real}(\omega)$ for $\hat{\theta}$ and $\hat{\phi}$ polarization are separately plotted in Figure 6. It can be seen that only Ant. A demonstrates pure polarization in the $\hat{\theta}$ direction due to its symmetrical geometry about the *y-z* plane, while all the other dipoles have comparable E_θ and E_ϕ components, especially above 5 GHz. For all the dipoles, the gain responses for the $\hat{\theta}$ polarization are almost the same in the *y-z* plane. Moreover, for Ants. B-D, the variations of $G_{real}(\omega)$ with the radiation direction are similar in the range of 0-10 GHz. With increasing θ, E_θ is observed to increase while E_ϕ decreases.

5 Current distributions

To investigate the differences in the polarization and $G_{real}(\omega)$ of the dipoles, the magnitudes in dB and directions of the current distributions at 3, 7, and 11 GHz are illustrated in Figures 7-9, and Figures 10-12, respectively. Hereby, only the current distributions on the lower parts of the dipoles

are presented. From Figures 7-9, it can be observed that the current densities at the edges of the dipoles, especially around the feed point, are much greater than those at the interior of the radiators. Obviously, the current distributions on Ant. A are kept symmetrical about the y-z plane at all the operating frequencies.

The difference in the $G_{real}(\omega)$ of Ants. A and C in the x-y plane can be explained from their current distributions. Figure 13 shows the top view of Ant. A or C, with the feed point located at the origin. Because of the large current densities on the plate edges among which the horizontal edges do not contribute to the radiation in the x-y plane, only the two vertical edges ($x = a$ or $(a - L)$, $y = 0$) can be considered as radiating elements, to approximate the far field radiation in the x-y plane. Each element has an independent radiating path in any specific radiation direction. In a reference plane as shown in Figure 13, the initial phases of the two radiating elements are obtained from (5) and (6), where c is the light speed, and ϕ is the radiation direction, assuming the initial phase in the voltage source as reference.

$$\text{Path 1: } \psi_1(\omega, \phi) = \omega \frac{a(1 - \cos\phi)}{c} \tag{5}$$

$$\text{Path 2: } \psi_2(\omega, \phi) = \omega \frac{(L - a)(1 + \cos\phi)}{c} \tag{6}$$

The above initial phases are plotted in Figure 14(a) for Ant. A ($a = 0.5L$), and Figure 14(b) for Ant. C ($a > 0.5L$). Apparently, by increasing a, the difference between $\psi_1(\omega)$ and $\psi_2(\omega)$ in the $\phi = 0^\circ$ direction decreases, and in the $\phi = 180^\circ$ direction increases. The variation of such phase difference greatly affects the bandwidth of $G_{real}(\omega)$. At an operating frequency f_{trough}, which results in $|\psi_1(2\pi f_{trough}) - \psi_2(2\pi f_{trough})| = \pi$ in the $\phi = 0^\circ$ or 180° direction, the $G_{real}(2\pi f_{trough})$ reaches a trough because the radiation from the two vertical edges is out of phase. With trivial deduction, the f_{trough} is obtained.

$$f_{trough} = \begin{cases} \dfrac{c}{4(L-a)} & ; \quad \phi = 0^\circ \\ \dfrac{c}{4a} & ; \quad \phi = 180^\circ \end{cases} \tag{7}$$

Therefore, the increased a of Ant. C raises the f_{trough} in the $\phi = 0^\circ$ direction, thus broadening the $G_{real}(\omega)$ in that direction, as shown in Figure 5(c). Similarly, the $G_{real}(\omega)$ of Ant. C in the $\phi = 180^\circ$ direction is narrowed due to the lowered f_{trough}.

Moreover, Ants. B and D have the similar trends as Ant. C, as shown in Figures 5(b) and 5(d), and can also be interpreted by (5), (6), and (7). For Ant. B, the far field radiation is not only due to the two vertical edges, but also contributed by the current densities on the oblique edges. Therefore, the effective L in (7) becomes smaller, and the f_{trough} in the $\phi = 0^\circ$ direction increases,

thus broadening the $G_{real}(\omega)$ in that direction. In the $\phi = 180^\circ$ direction, the f_{trough} does not change greatly because of the fixed a, but the deeper null of $G_{real}(\omega)$ at f_{trough} as shown in Figure 5(b) decreases the bandwidth of the $G_{real}(\omega)$. In the case of Ant. D, the f_{trough} in both the $\phi = 0^\circ$ and $\phi = 180^\circ$ directions is almost the same to that of Ant. B, as a of Ant. D is also fixed, and the shorting-pin introduces more vertical currents between the feed point and the shorting pin at high frequencies as shown in Figure 12(d), thus reducing the effective L. However, in contrast to Ant. B whose null of $G_{real}(\omega)$ in the $\phi = 180^\circ$ is below -25 dBi, the $G_{real}(\omega)$ of Ant. D is stabler with frequency due to its shallow null with a value of about -5 dBi. It may be caused by the unbalanced radiation of the two vertical edges at high frequencies. From Figure 9(d), the current density on the shorted vertical edge is weaker than that on the other one, which alleviates the cancellation of the out-of-phase radiation from these two edges at the f_{trough}. In addition, a part of the radiation from the shorted edge is canceled by itself because of the currents with opposite directions on that edge, as can be seen in Figure 12(d). It is another reason of the weaker cancellation between the two radiation elements.

6 Time-domain performances

As the time-domain performance of an antenna is important in UWB applications, the radiated pulses in the x-y plane are investigated. Two schemes, namely the single-band scheme and multi-band scheme, with different source pulses are studied for UWB applications. In the single-band scheme, the voltage source may be a monocycle in the form of (8), where $\sigma = 50$ ps. In the multi-band scheme, the voltage source can be a series of modulated Gaussian pulses, each having the same bandwidth but different central frequencies, as defined in (9), where $\sigma = 1366$ ps is chosen so as to obtain a 500 MHz 10dB-bandwidth for each pulse. Therefore, the spectrum of (9) covers the entire UWB band.

$$V_s(t) = t \exp[-(\frac{t}{\sigma})^2] \tag{8}$$

$$V_m(t) = \sum_{n=0}^{14} \sin[2\pi(3.35 \times 10^9 + n \times 0.5 \times 10^9)(t - nT)] \exp[-(\frac{t - nT}{\sigma})^2] \tag{9}$$

The resulting time-domain electric field in the x-y plane is obtained by XFDTD, and plotted in Figure 15 for the single-band scheme, and Figures 16-19 for the multi-band scheme. All the pulses are obtained at an observation point 655mm away from the dipole. It is clear that, for all the dipoles, the radiated pulses in both single-band and multi-band schemes change with the radiation direction. Such variation is directly determined by the stability of $G_{real}(\omega)$ in terms of the radiation direction.

Taking Ant. C for example, its stable gain in the range of $|\phi| \leq 60^\circ$, as shown in Figure 5(c), leads to the nearly unchanged waveforms for both the single-band scheme in Figure 15(c) and the multi-band scheme in Figures 18(a) and 18(b). On the other hand, when $60^\circ \leq |\phi| \leq 180^\circ$, the waveforms change a lot due to the varied gain. Similar phenomenon can be observed for the other three dipoles.

7 Conclusions

Four planar dipoles have been studied and compared in terms of impedance as well as radiation characteristics including the realized gain and polarization. Their equivalent monopoles have been investigated experimentally, to verify the simulated input impedance, and realized gain in the $\theta = \phi = 90^\circ$ direction. The current distributions at three typical operating frequencies have been used to interpret the radiation features. Particularly, the stability of the realized gain responses against the radiation direction has been studied. The time-domain responses of the dipoles in the transmitting mode have been investigated for the single-band and multi-band schemes in UWB applications. In particular, the variation of the time-domain waveforms with different radiation directions have been discussed. Four points have been concluded from this study.

- Ant. C features the broadest impedance bandwidth among the four dipoles.
- Compared with Ant. A, other three dipoles demonstrate better radiation stability against the direction when $\theta = 90^\circ$ and $|\phi| \leq 60^\circ$, but worse one when $\theta = 90^\circ$ and $60^\circ \leq |\phi| \leq 180^\circ$.
- In the y-z plane, all the dipoles demonstrate similar radiation performance except that the radiation of Ant. A has no E_ϕ component.
- The variation of radiated pulses with different directions is determined by the radiation stability. Good stability against the radiation direction results in nearly unchanged pulses in both single-band and multi-band schemes.

References

[1] Zhi Ning Chen, Xuan Hui Wu, Hui Feng Li, Ning Yang, M.Y.W. Chia: 'Considerations for Source Pulses and Antennas in UWB Radio Systems' *IEEE transactions on Antennas and Propagation*, 2004, 52, (7), pp. 1739-1748.

[2] Xuan Hui Wu, Zhi Ning Chen, M.Y.W. Chia: 'Note on Antenna Design in UWB Wireless Communication Systems.', *2003 IEEE Conference on Ultra Wideband Systems and Technologies*, Reston, Virginia, USA, Nov. 16-19, 2003, pp. 503-507.

[3] Narayan Prasad Agrawall, Girish Kumar, K.P. Ray: 'Wide-Band Planar Monopole Antennas.' IEEE Transactions on Antennas and Propagation, 1998, 46, (2), pp. 294-295.

[4] M.J. Ammann: 'Impedance Bandwidth of the Square Planar Monopole.' Microwave and Optical Technology Letters, 2000, 24, (3), pp. 185-187.

[5] Zhi Ning Chen: 'Impedance characteristics of planar bow-tie-like monopole antennas.' Electronics Letters, 2000, 36, (13), pp. 1100-1101.

[6] M.J. Ammann, Zhi Ning Chen: 'A Wide-Band Shorted Planar Monopole With Bevel.' IEEE Transaction on Antennas and Propagation, 2003, 51, (4), pp. 901-903.

[7] Z.N. Chen, M.Y.W. Chia, M.J. Ammann: 'Optimization and Comparison of Broadband Monopoles.', *IEE Proc.-Microw. Antennas Propag.*, 2003, 150, (6), pp. 429-435.

[8] Zhi Ning Chen, Xuan Hui Wu, Ning Yang, M.Y.W. Chia: 'Planar Square Monopoles for UWB Radio Systems.', *2003 Asia-Pacific Microwave Conference*, Seoul, Korea, Nov. 4-7, 2003, pp. 1632-1635.

[9] Taeyoung Yang, Seong-Youp Suh, Randall Nealy, William A. Davis, and Warren L. Stutzman: 'Compact Antennas for UWB Applications', *2003 IEEE Conference on Ultra Wideband Systems and Technologies*, Reston, Virginia, USA, Nov. 16-19, 2003, pp. 205-208.

[10] Hans Grepory Schantz: 'Bottom Fed Planar Elliptical UWB Antennas', *2003 IEEE Conference on Ultra Wideband Systems and Technologies*, Reston, Virginia, USA, Nov. 16-19, 2003, pp. 219-223.

[11] Kwan-Ho Kim, Sung-Bae Cho, Young-Jin Park, Han-Gyu Park: 'Novel Planar Ultra Wideband Stepped-Fat Dipole Antenna', *2003 IEEE Conference on Ultra Wideband Systems and Technologies*, Reston, Virginia, USA, Nov. 16-19, 2003, pp. 508-512.

[12] X.H. Wu, Z.N. Chen, N. Yang: 'Optimization of Planar Diamond Antenna for Single/Multi-band UWB Wireless Communications', *Microwave and Optical Technology Letters*, 2004, 42, (6), pp. 451-455.

Table 1: Impedance bandwidth of $|S_{11}(\omega)| < -10$dB

Antenna	Ant. A	Ant. B	Ant. C	Ant. D
Bandwidth (GHz)	3.60-8.21	3.40-10.17	3.61-15.30	2.87-10.04

Table 2: ΔG_{max}, $\theta = 90^\circ$ and $|\phi| \leq 60^\circ$

Antenna	Ant. A	Ant. B	Ant. C	Ant. D
dB@GHz	5.84@10.43	1.43@6.72	0.79@5.74	2.07@10.60

Table 3: ΔG_{max}, $\theta = 90^\circ$ and $60^\circ \leq |\phi| \leq 180^\circ$

Antenna	Ant. A	Ant. B	Ant. C	Ant. D
dB@GHz	8.31@10.60	29.62@9.90	20.71@7.94	10.83@9.54

List of Tables

List of Figures

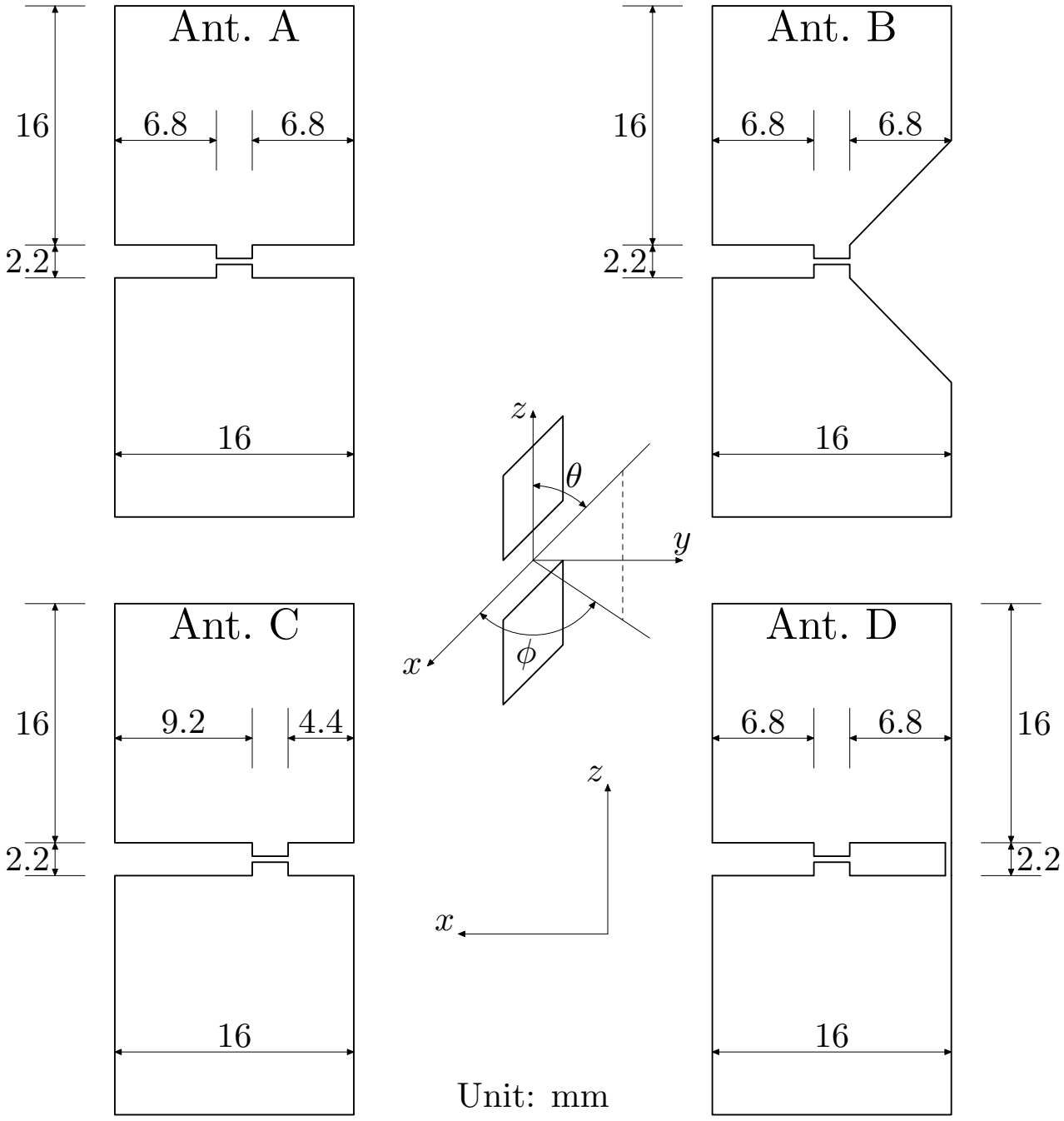

Figure 1: Antenna Geometries

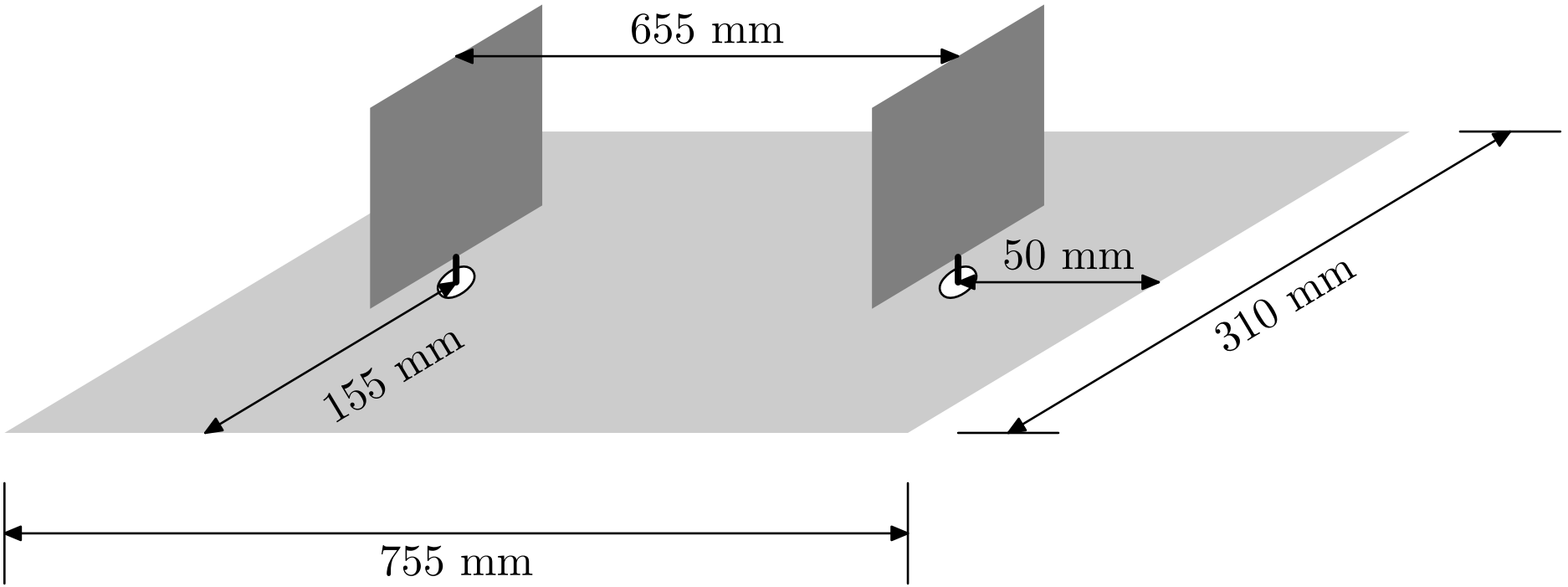

Figure 2: Measurement set-up

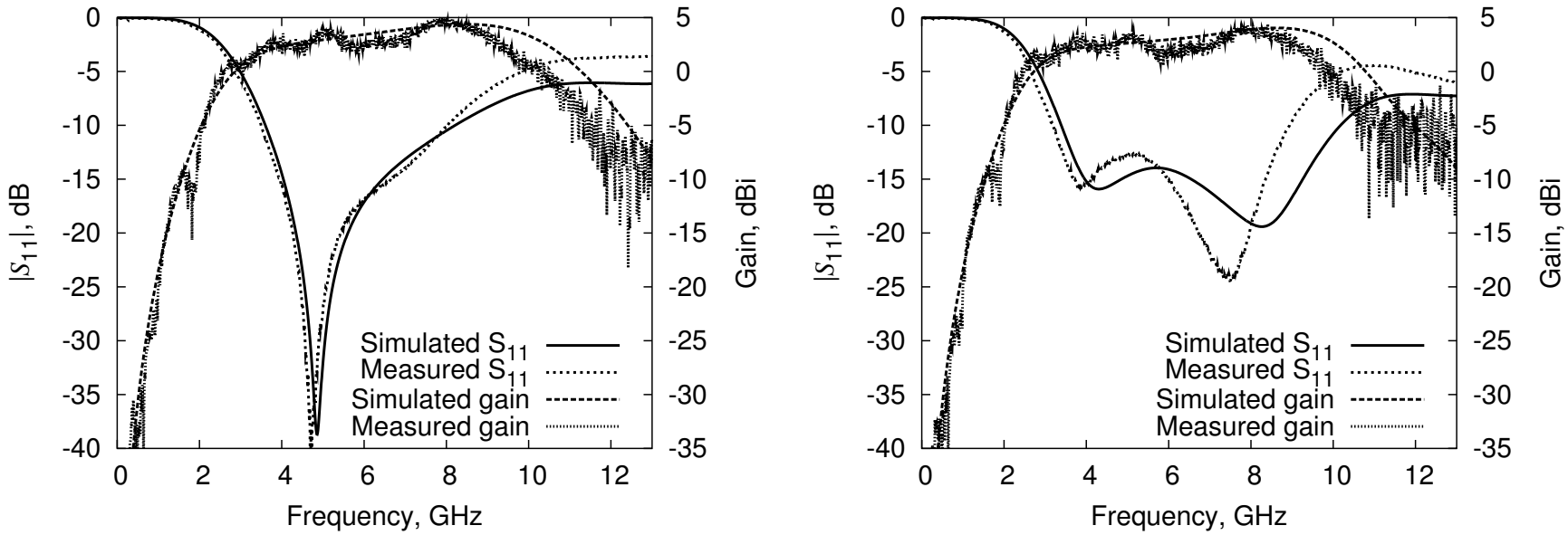

(a) Ant. A

(b) Ant. B

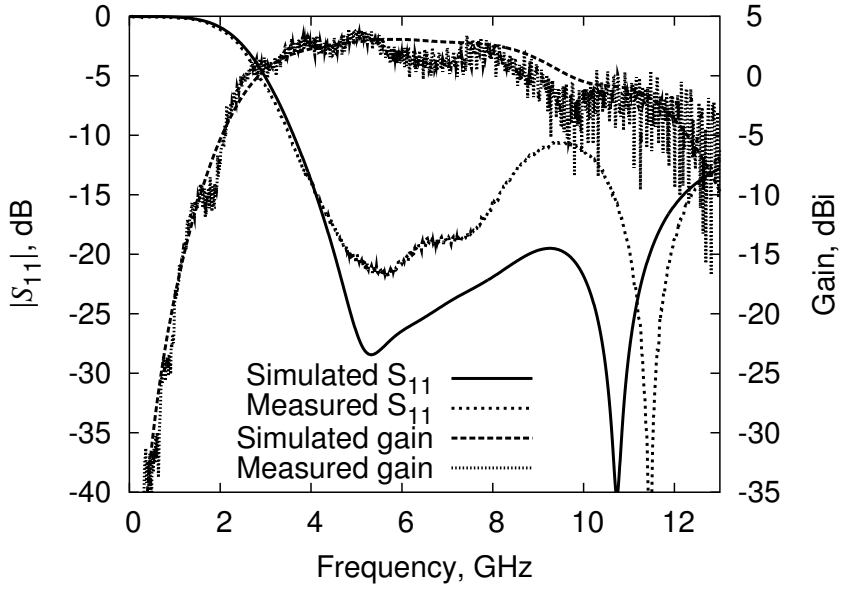

(c) Ant. C

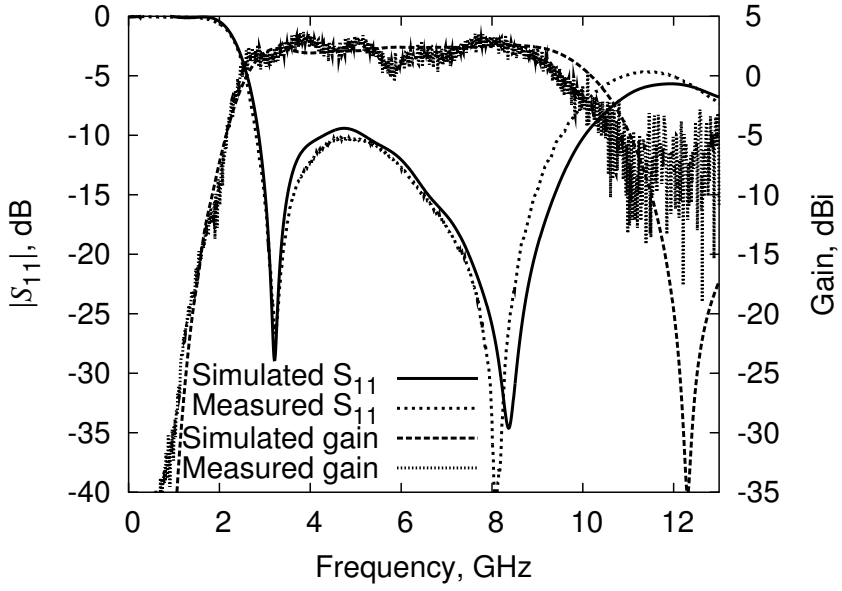

(d) Ant. D

Figure 3: Comparison of simulation and measurement

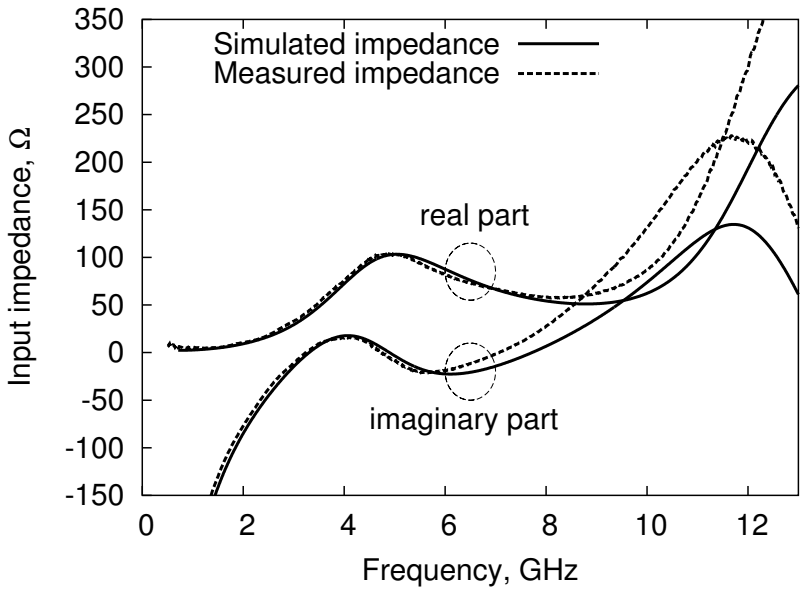

(a) Ant. A

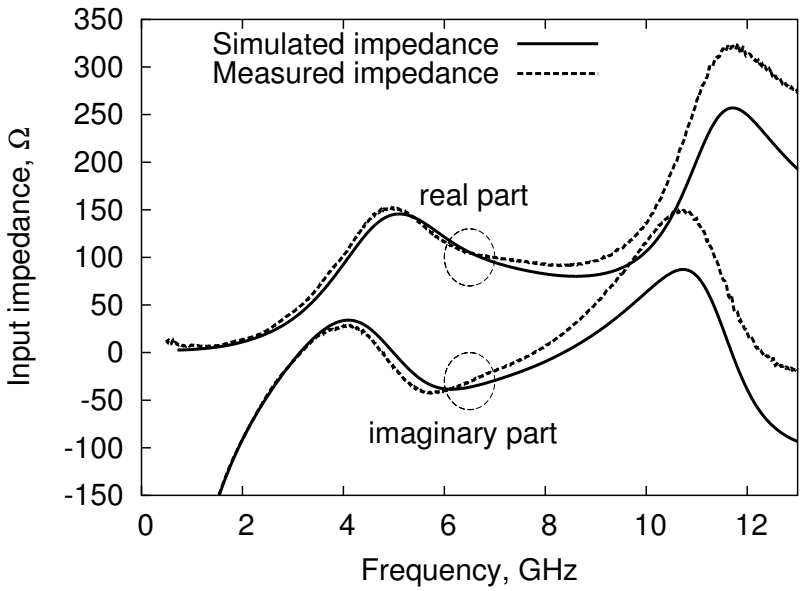

(b) Ant. B

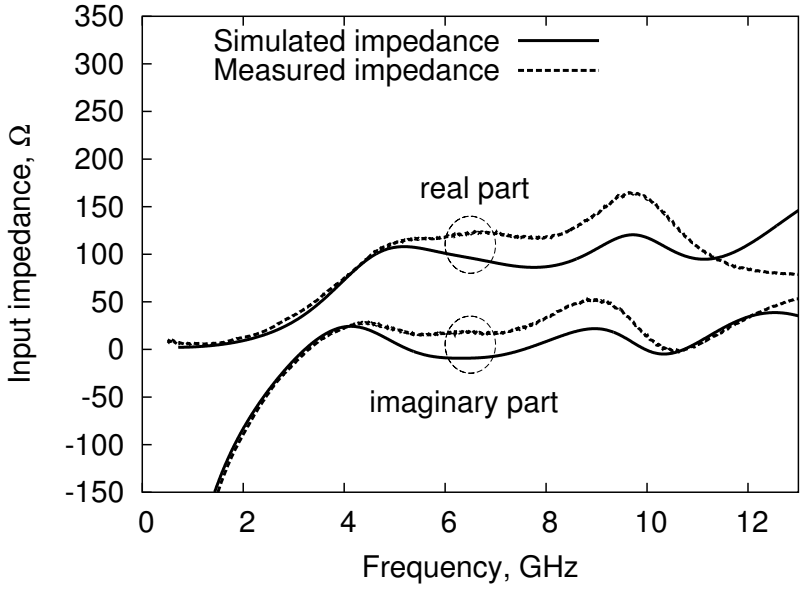

(c) Ant. C

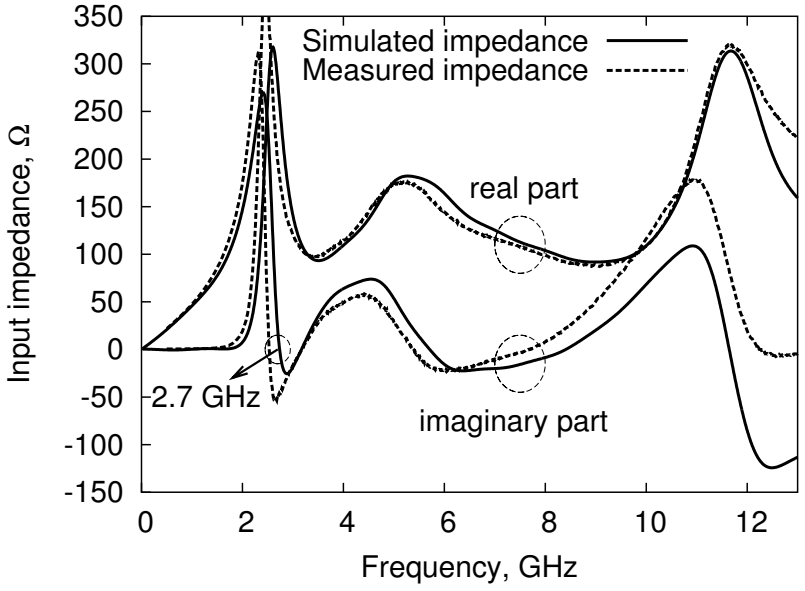

(d) Ant. D

Figure 4: Input impedance

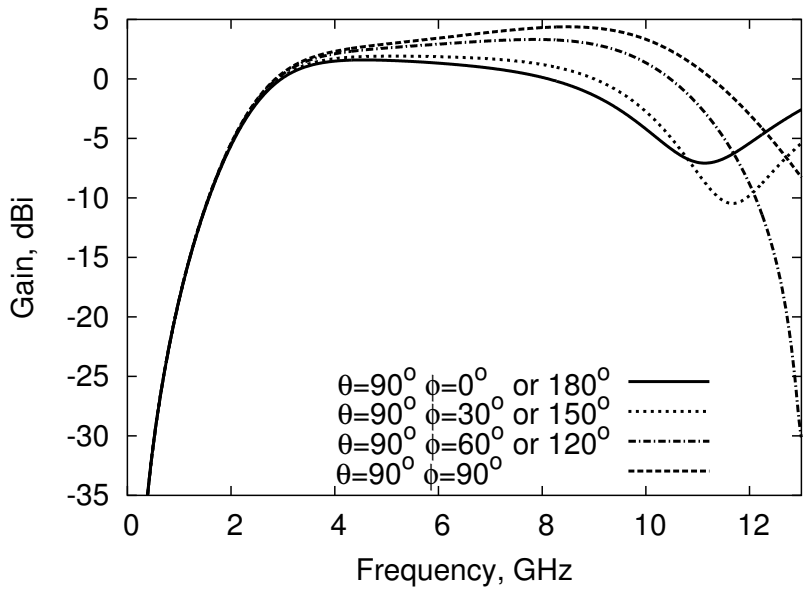

(a) Ant. A

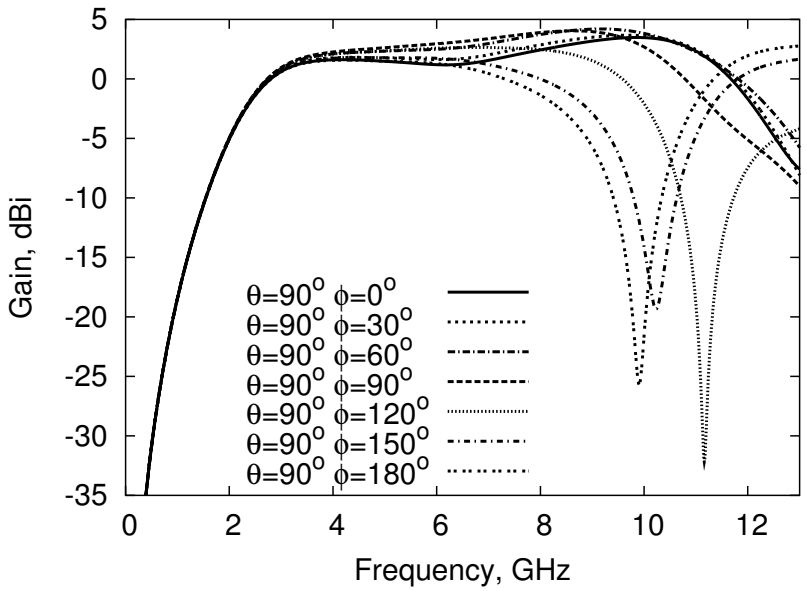

(b) Ant. B

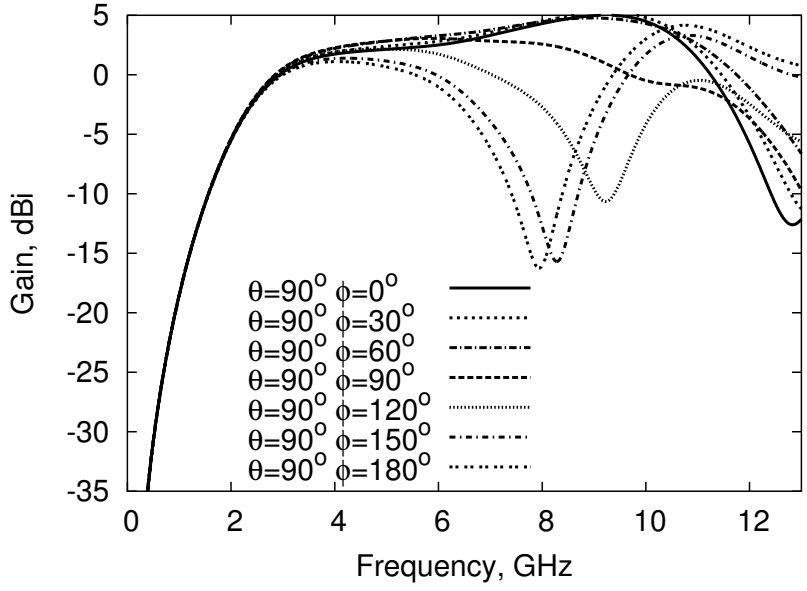

(c) Ant. C

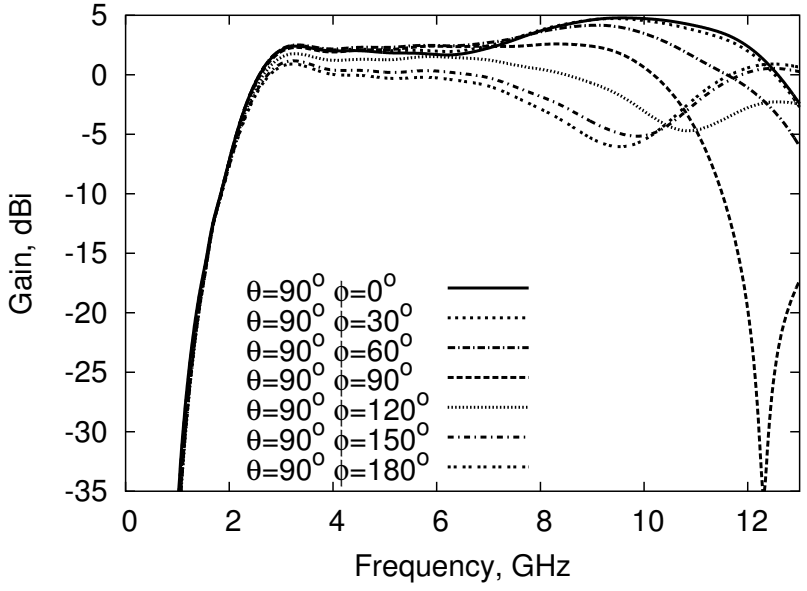

(d) Ant. D

Figure 5: Realized gain in x-y ($\theta = 90°$) plane

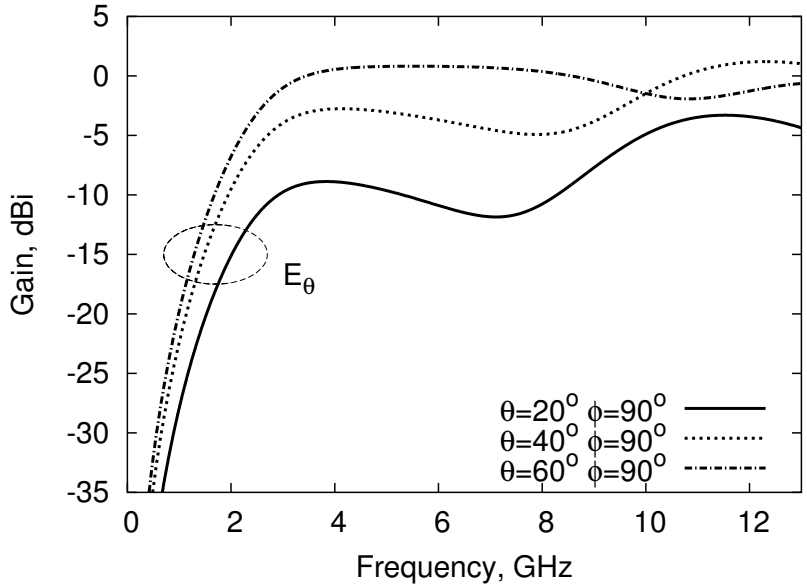

(a) Ant. A

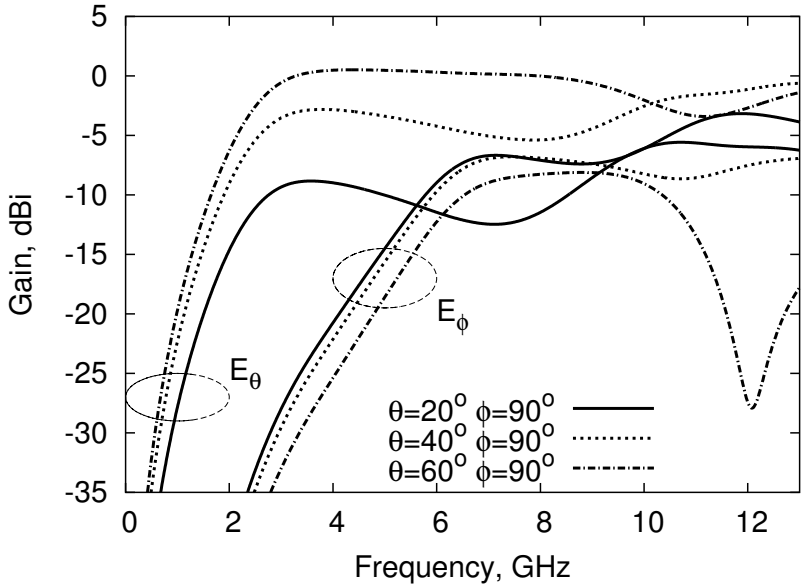

(b) Ant. B

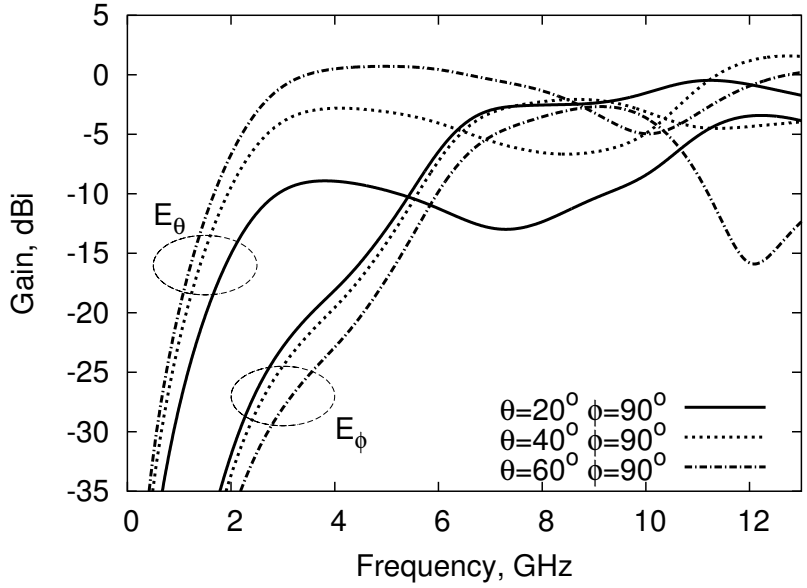

(c) Ant. C

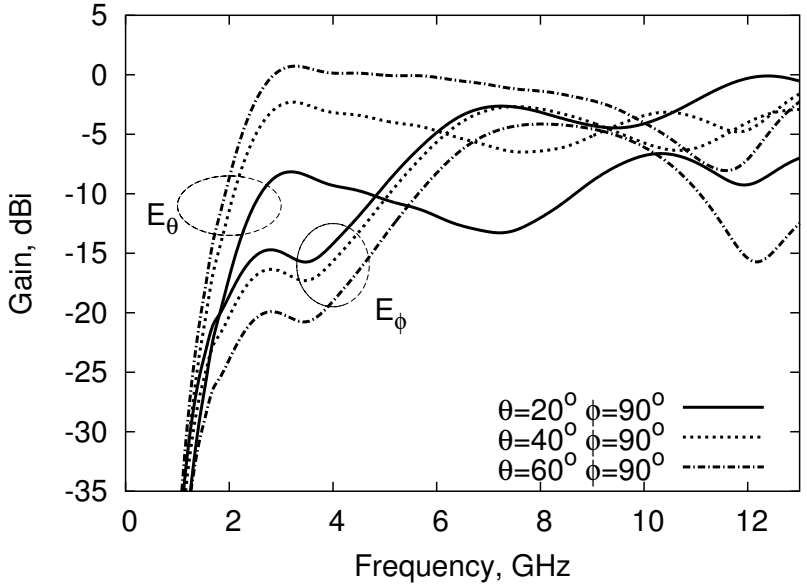

(d) Ant. D

Figure 6: Realized gain in y-z ($\phi = 90°$) plane

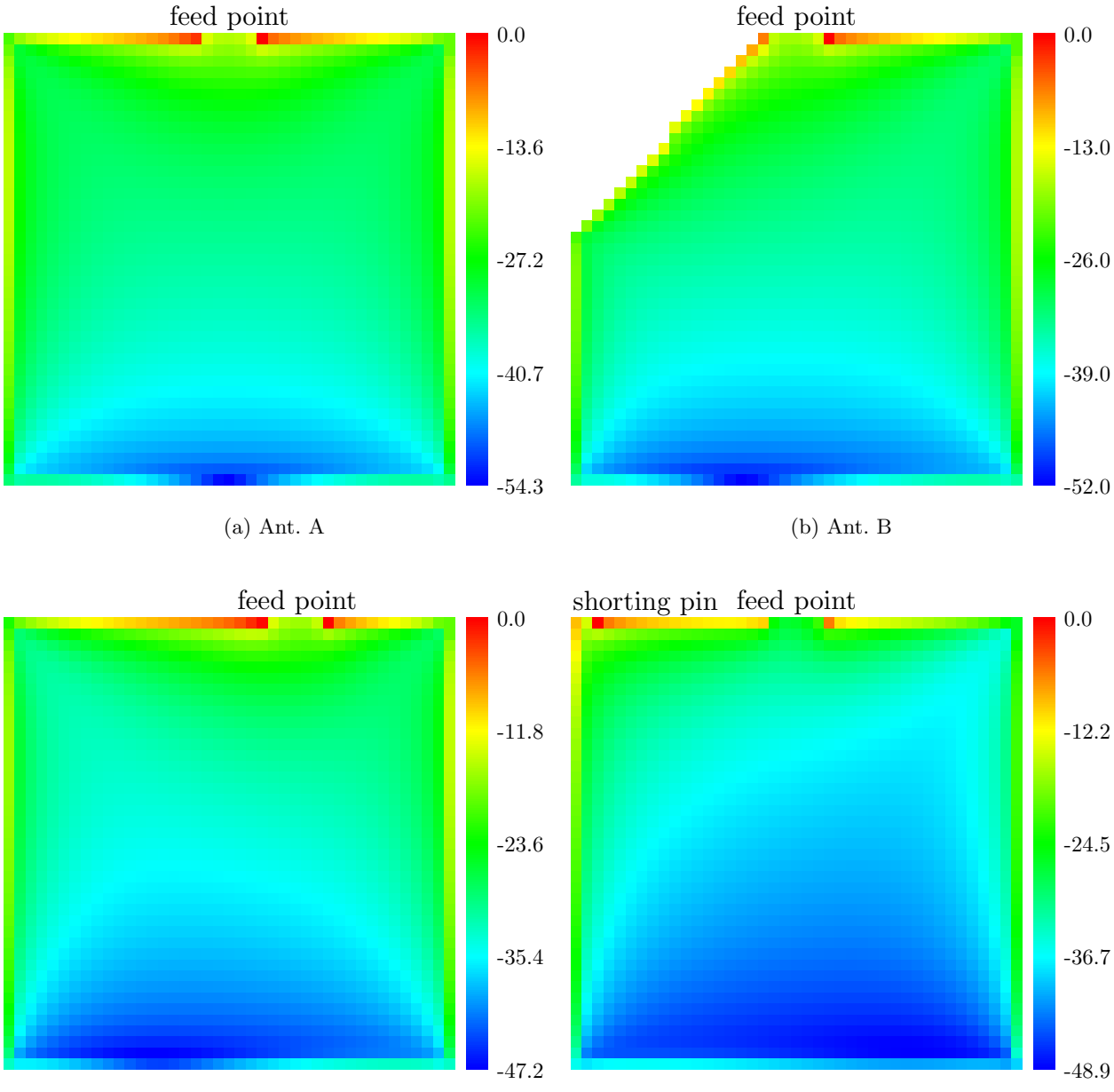

(a) Ant. A

(b) Ant. B

(c) Ant. C

(d) Ant. D

Figure 7: Magnitudes of the current distributions at 3 GHz

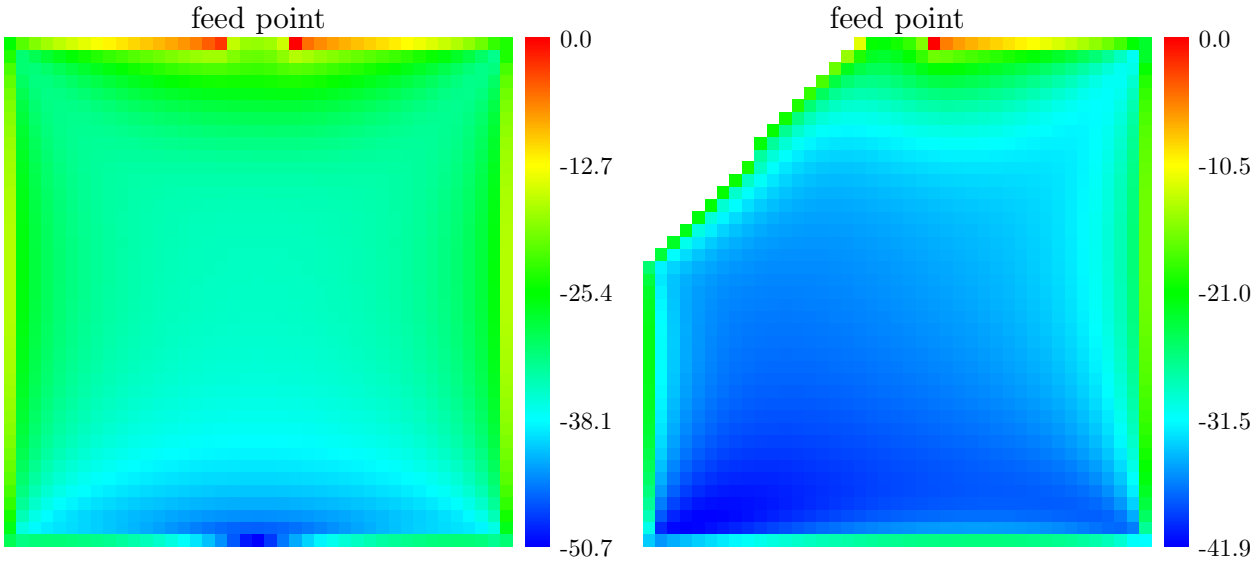

(a) Ant. A

(b) Ant. B

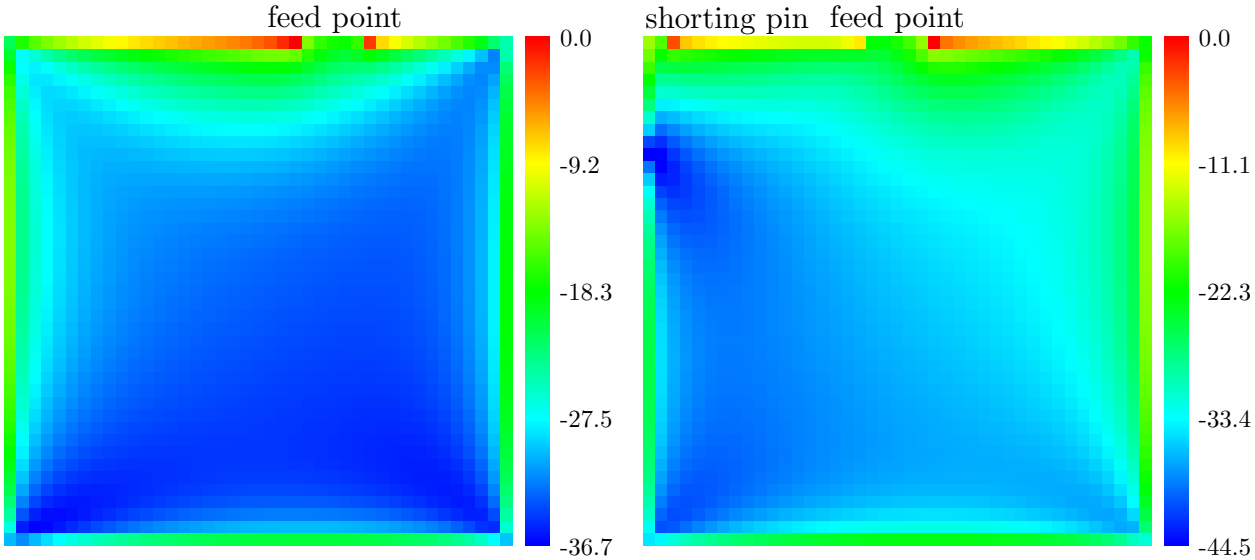

(c) Ant. C

(d) Ant. D

Figure 8: Magnitudes of the current distributions at 7 GHz

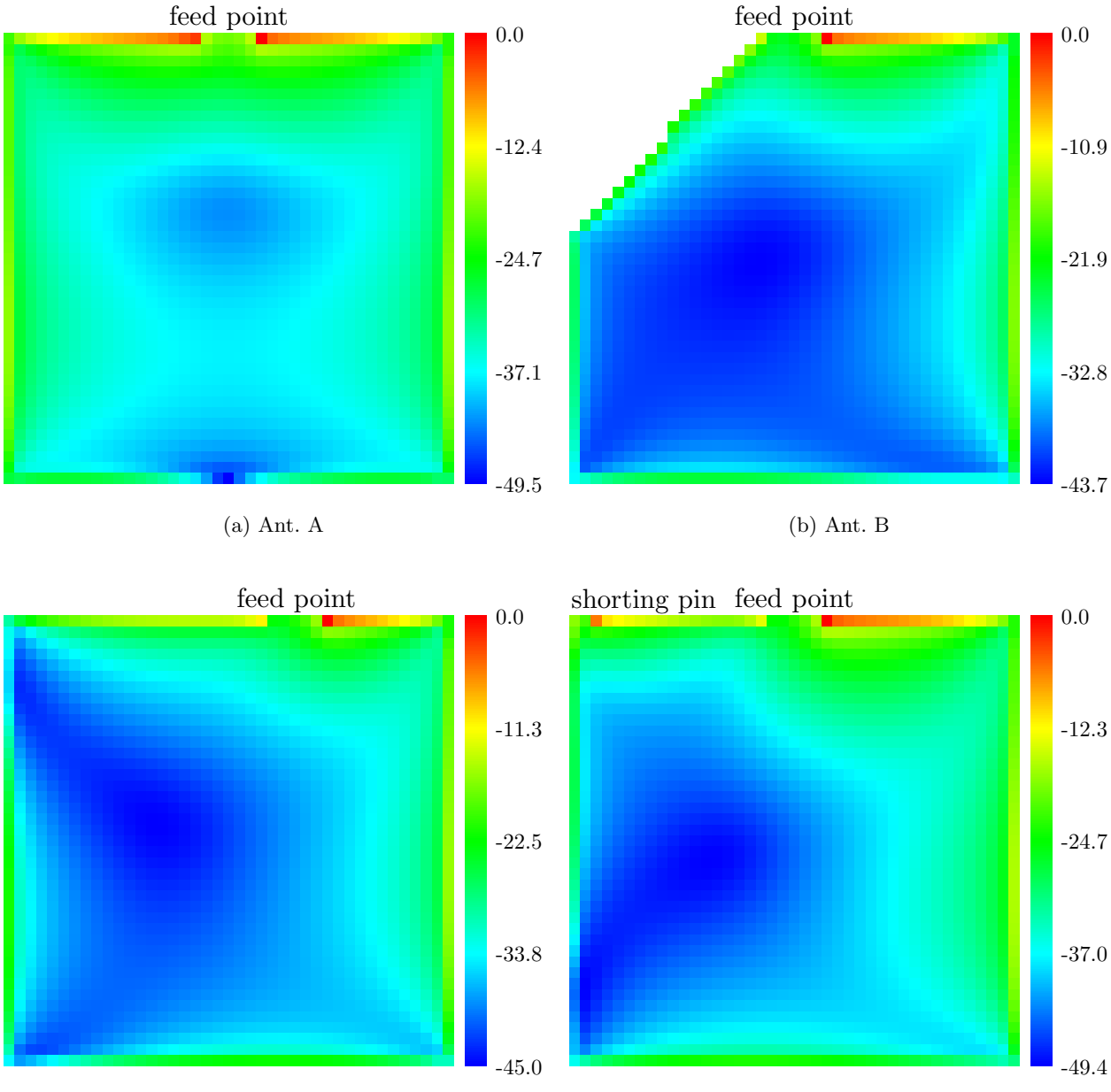

(a) Ant. A

(b) Ant. B

(c) Ant. C

(d) Ant. D

Figure 9: Magnitudes of the current distributions at 11 GHz

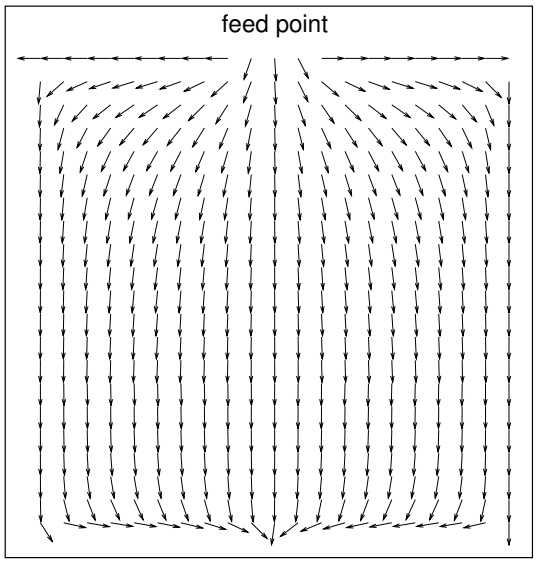

(a) Ant. A

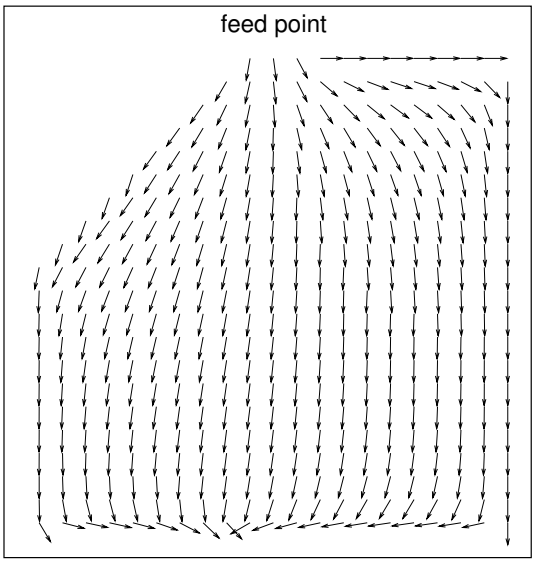

(b) Ant. B

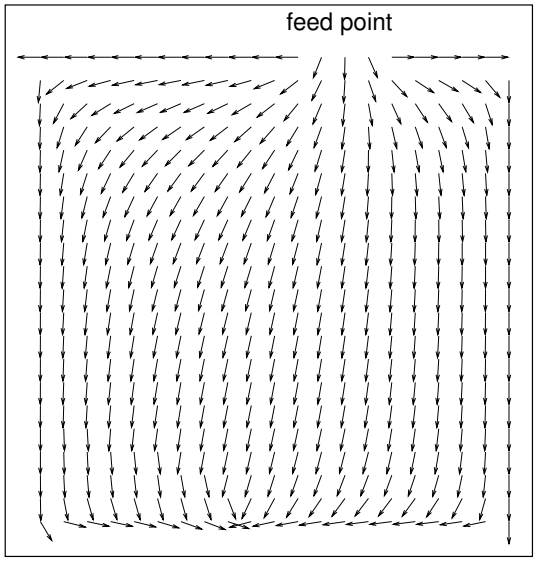

(c) Ant. C

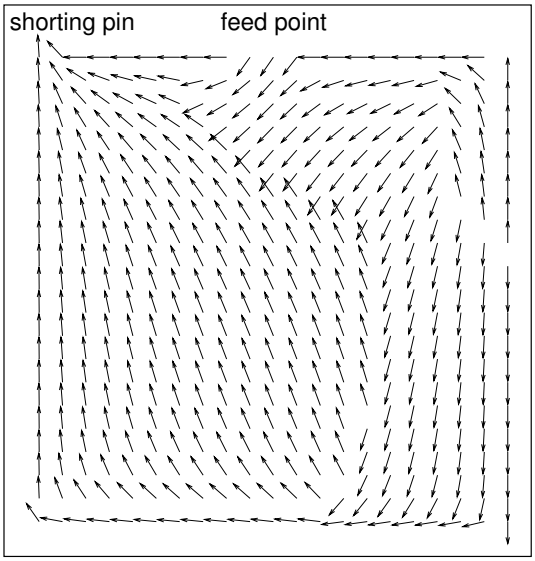

(d) Ant. D

Figure 10: Directions of the current distributions at 3 GHz

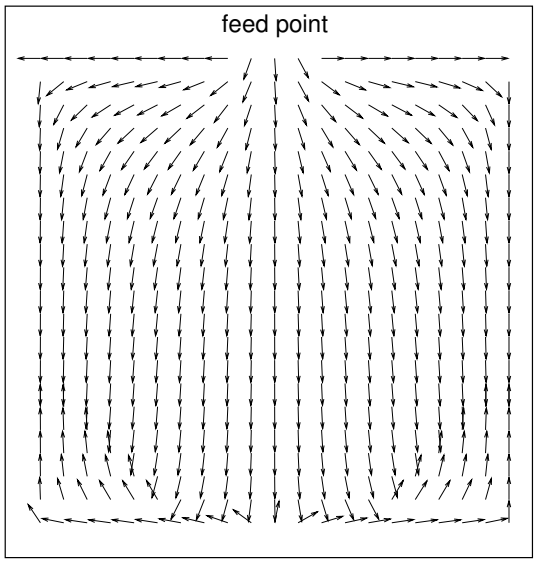

(a) Ant. A

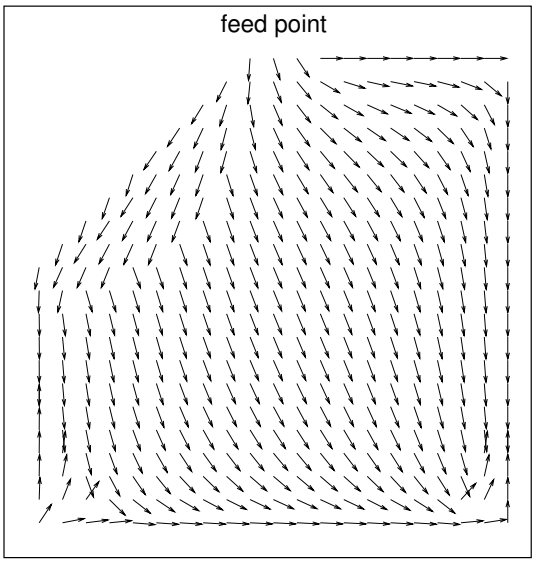

(b) Ant. B

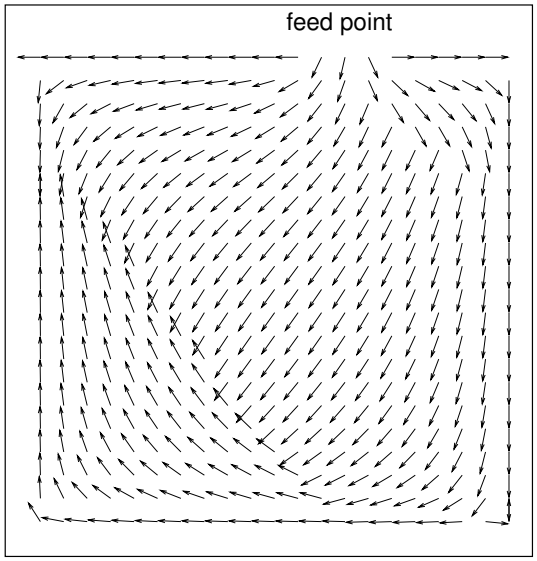

(c) Ant. C

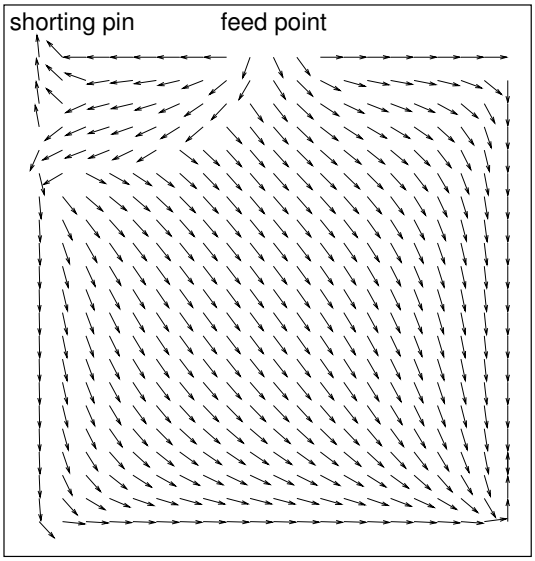

(d) Ant. D

Figure 11: Directions of the current distributions at 7 GHz

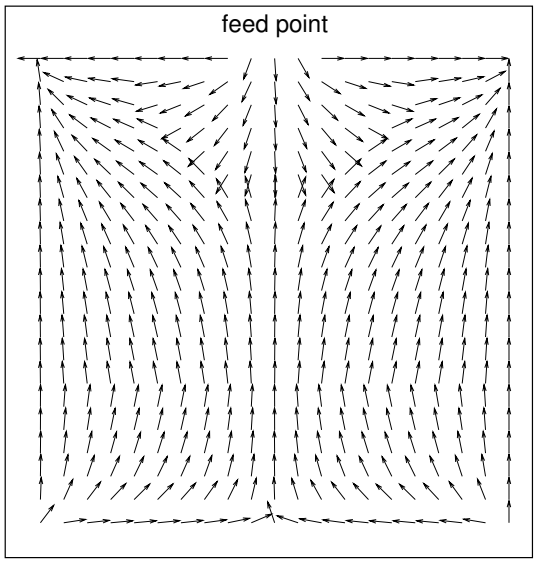

(a) Ant. A

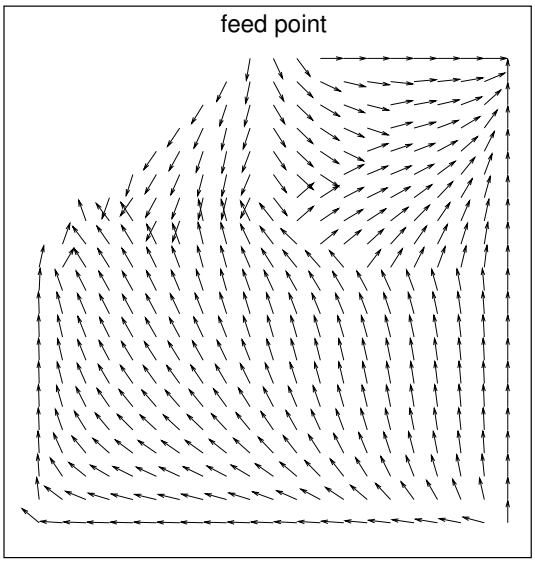

(b) Ant. B

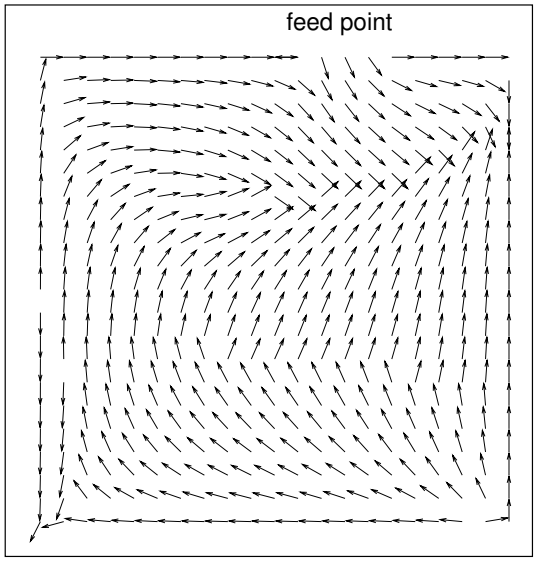

(c) Ant. C

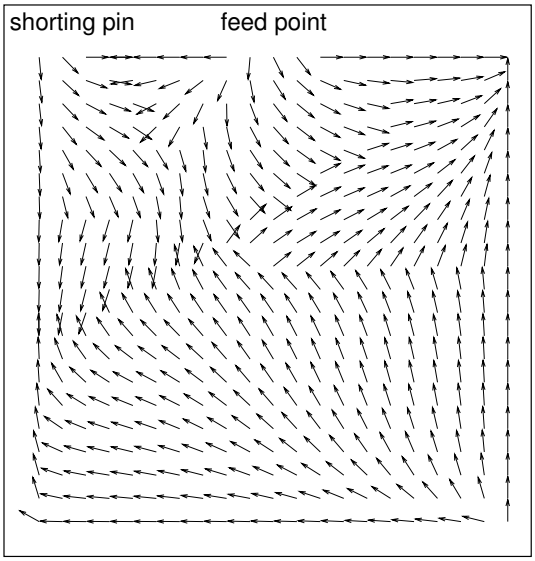

(d) Ant. D

Figure 12: Directions of the current distributions at 11 GHz

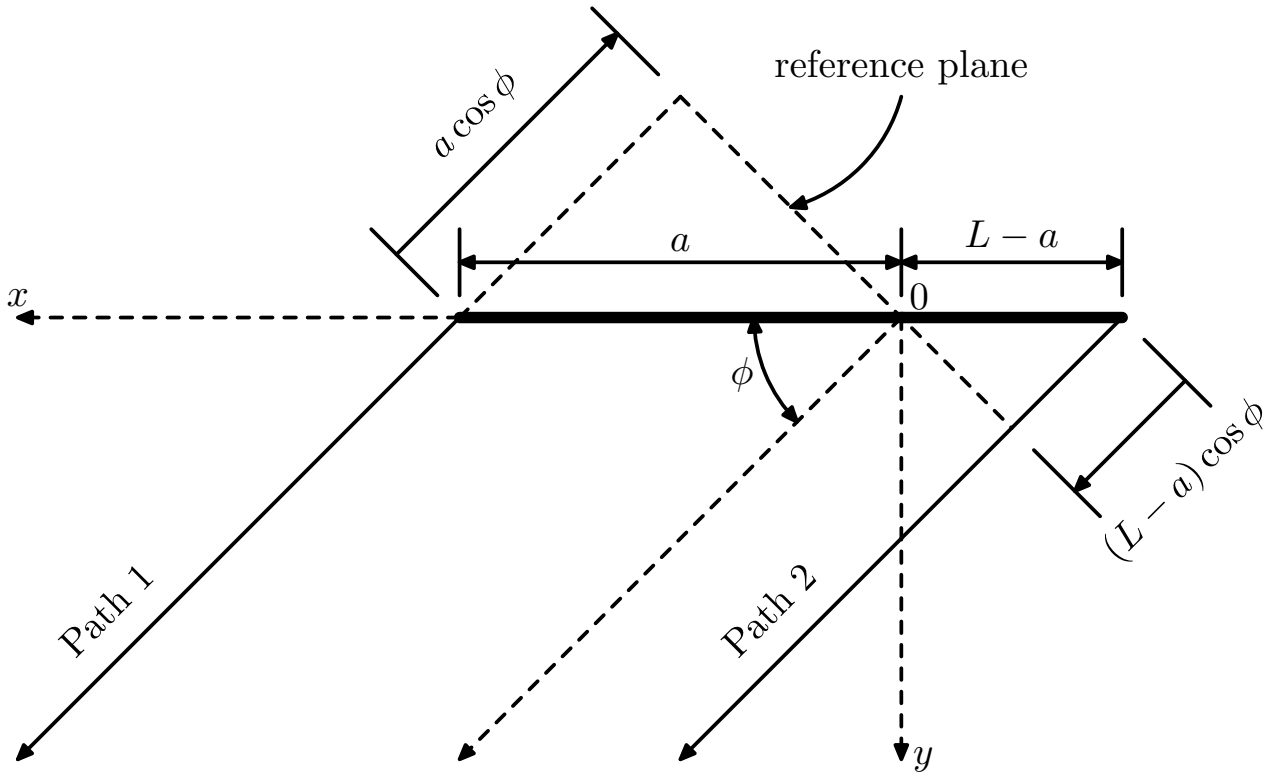

Figure 13: Top view of a radiating planar antenna

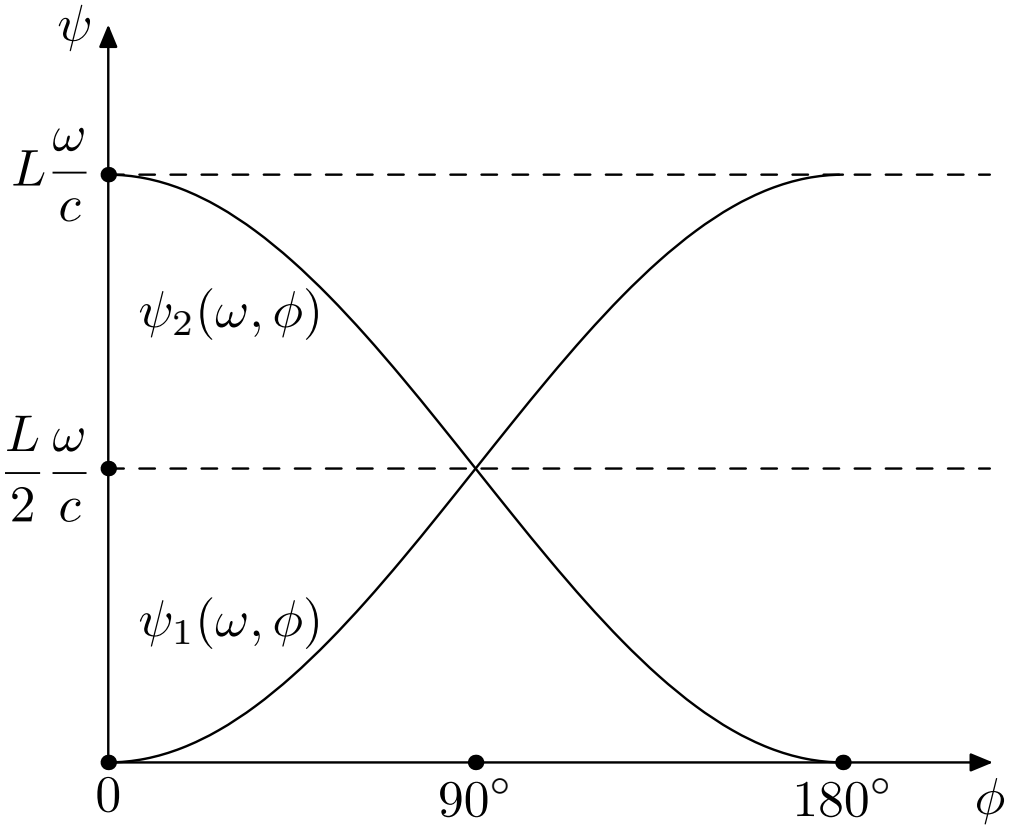

(a) $a = 0.5L$

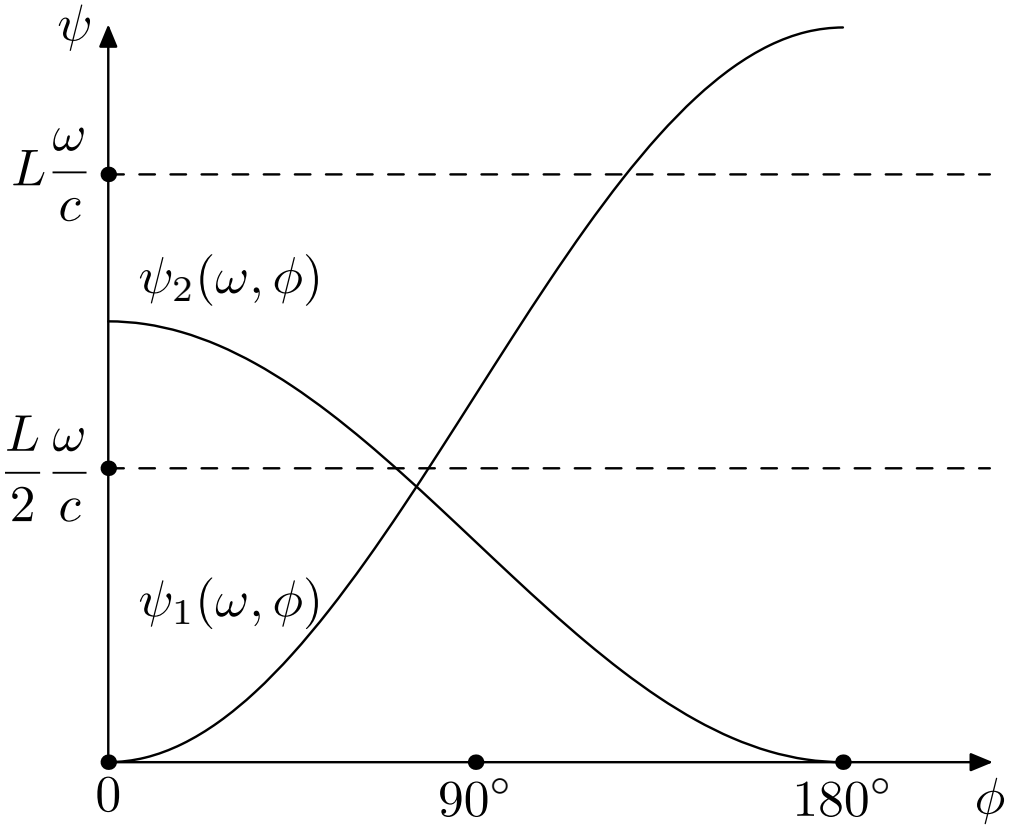

(b) $a > 0.5L$

Figure 14: Initial phases of different radiating elements in the reference plane

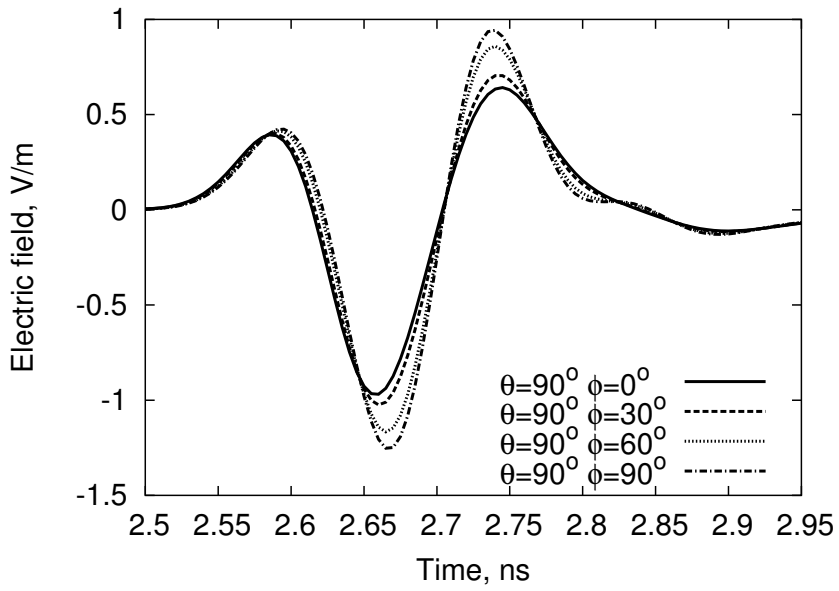

(a) Ant. A

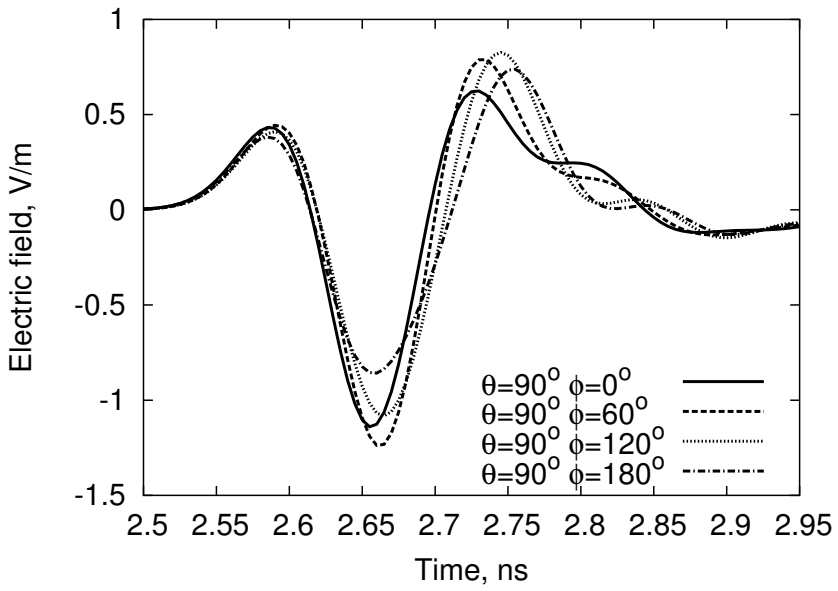

(b) Ant. B

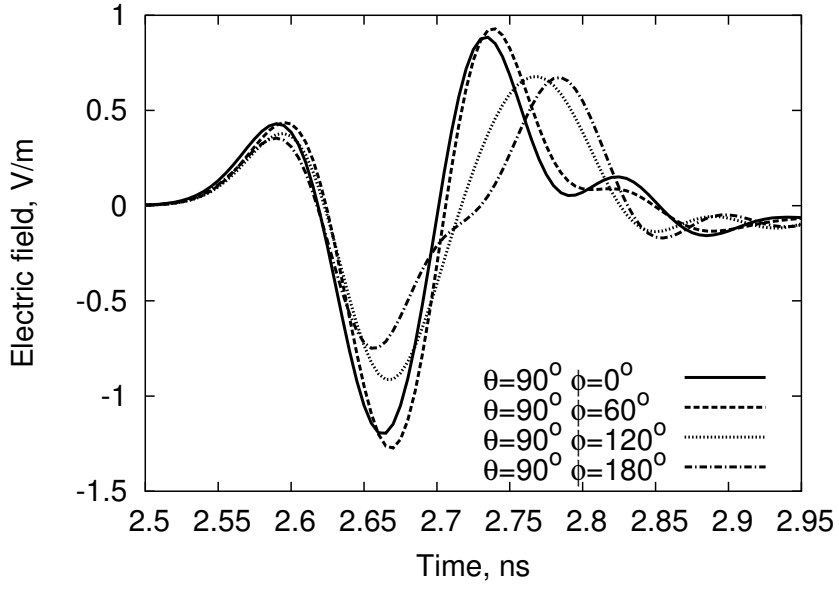

(c) Ant. C

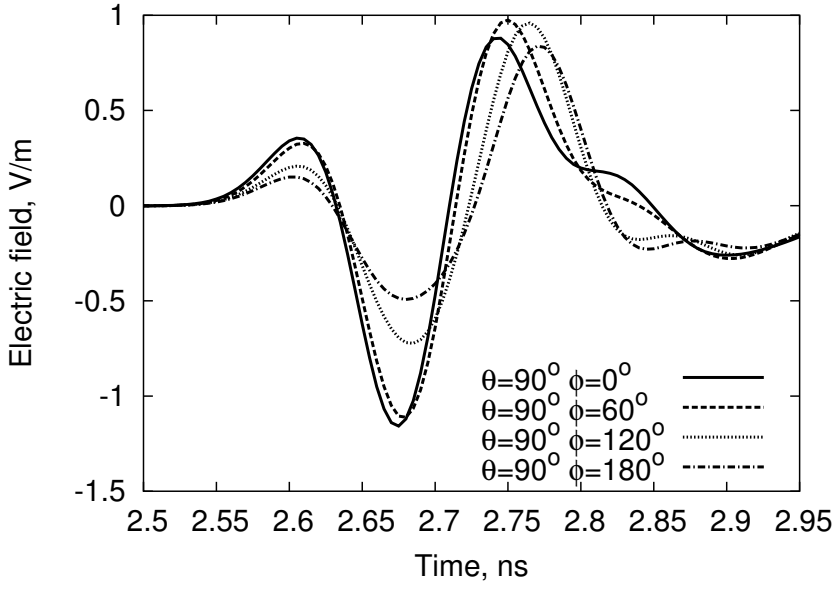

(d) Ant. D

Figure 15: Radiated pulses in a single-band scheme

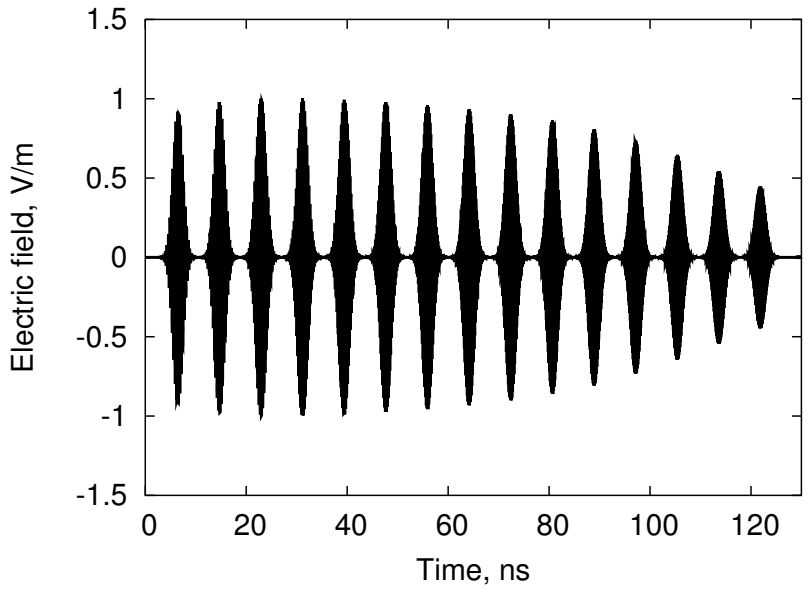

(a) $\theta = 90°, \phi = 0°$

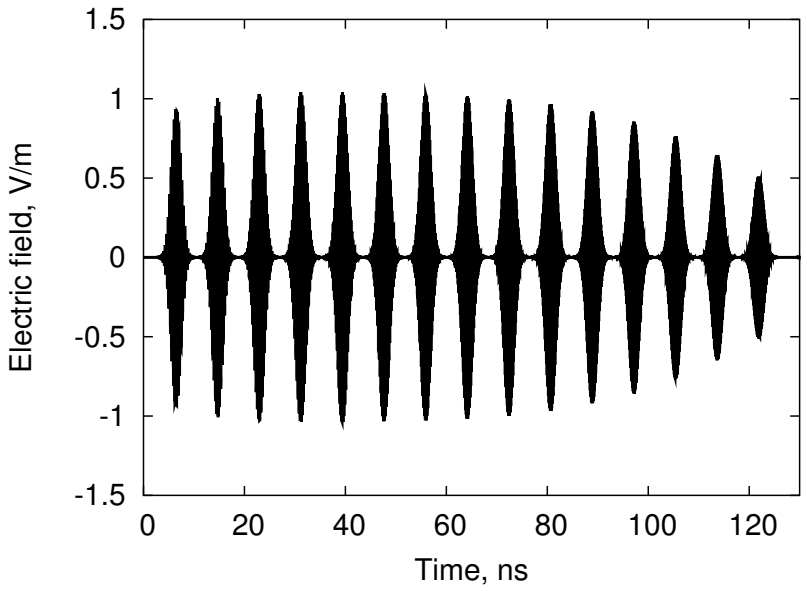

(b) $\theta = 90°, \phi = 30°$

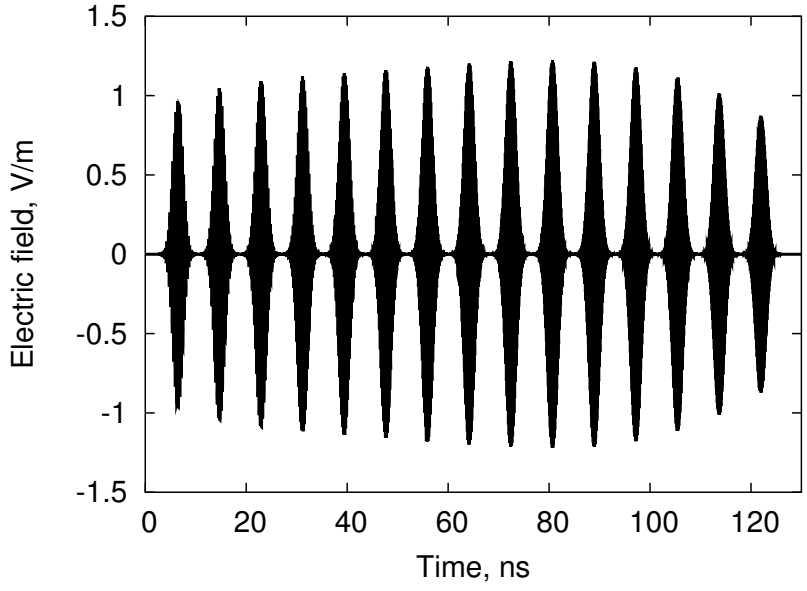

(c) $\theta = 90°, \phi = 60°$

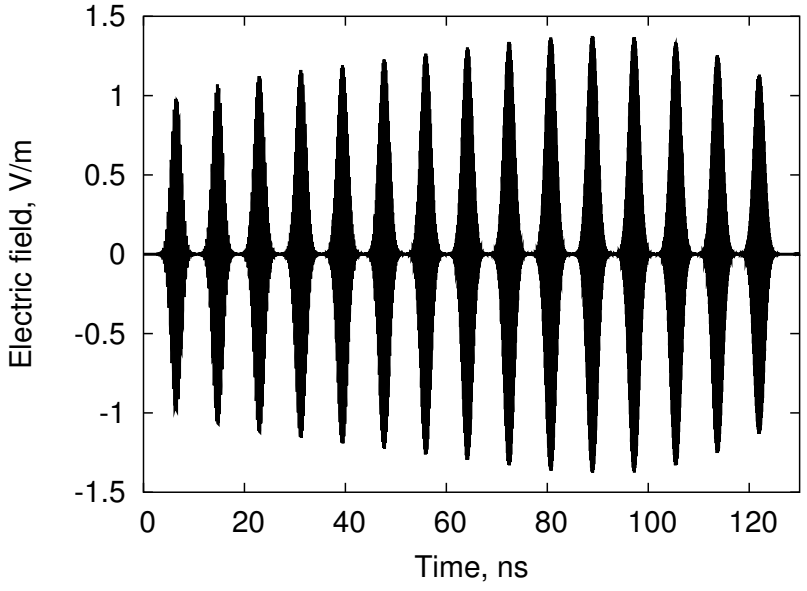

(d) $\theta = 90°, \phi = 90°$

Figure 16: Radiated pulses of Ant. A in a multi-band scheme

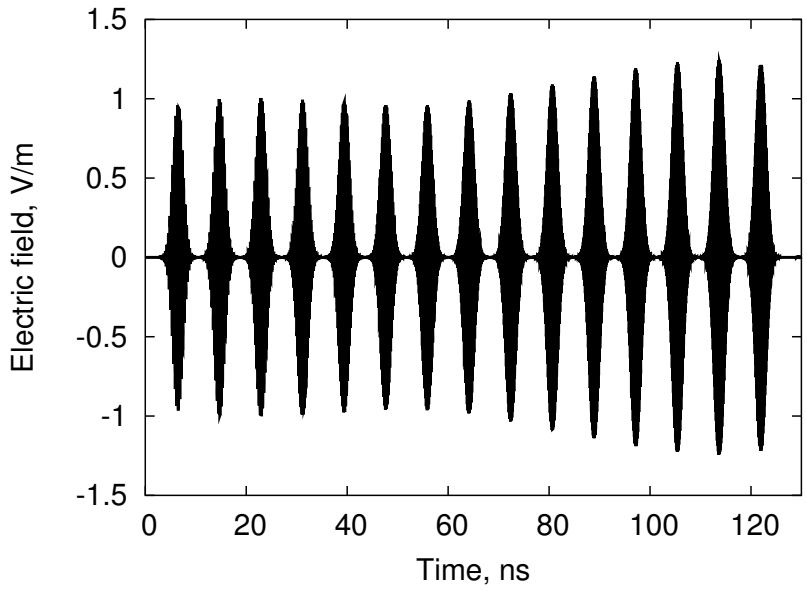

(a) $\theta = 90°, \phi = 0°$

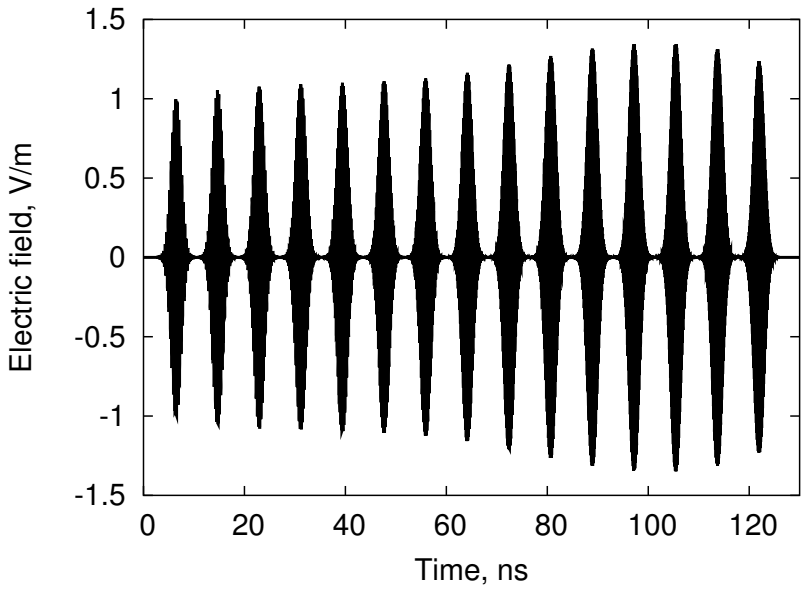

(b) $\theta = 90°, \phi = 60°$

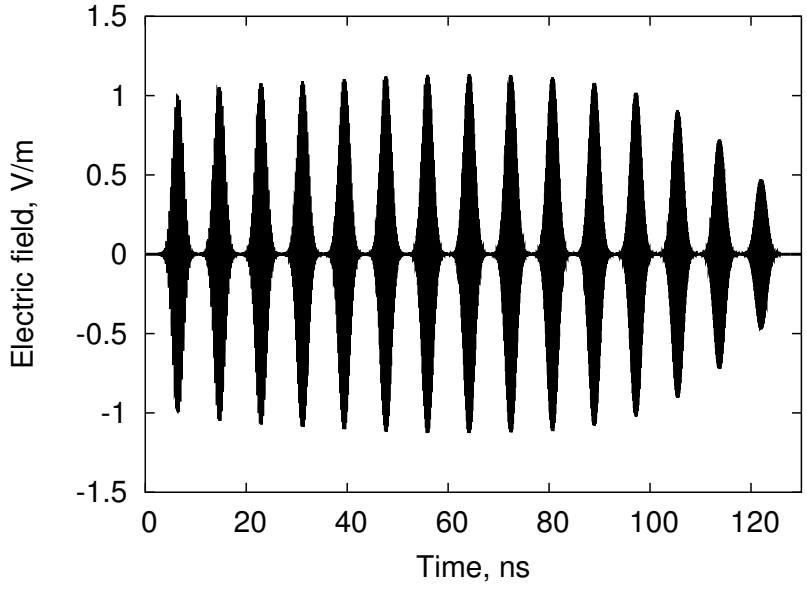

(c) $\theta = 90°, \phi = 120°$

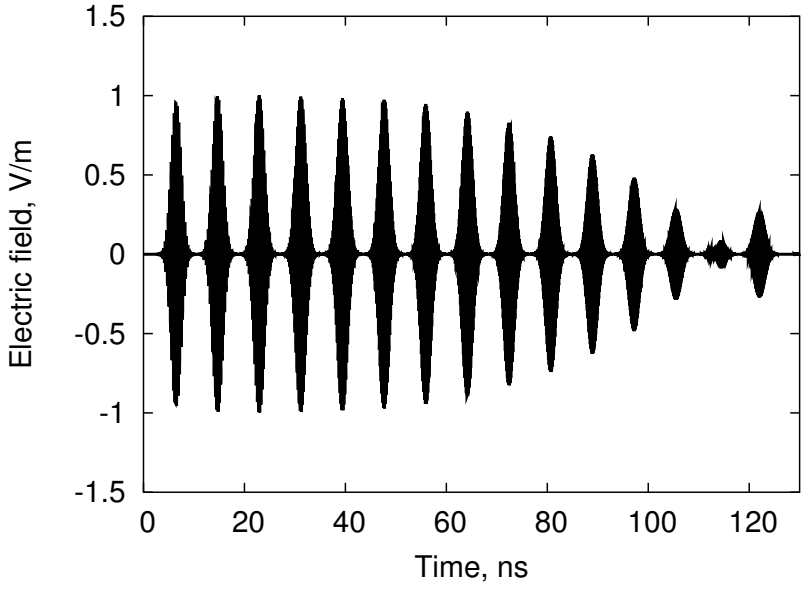

(d) $\theta = 90°, \phi = 180°$

Figure 17: Radiated pulses of Ant. B in a multi-band scheme

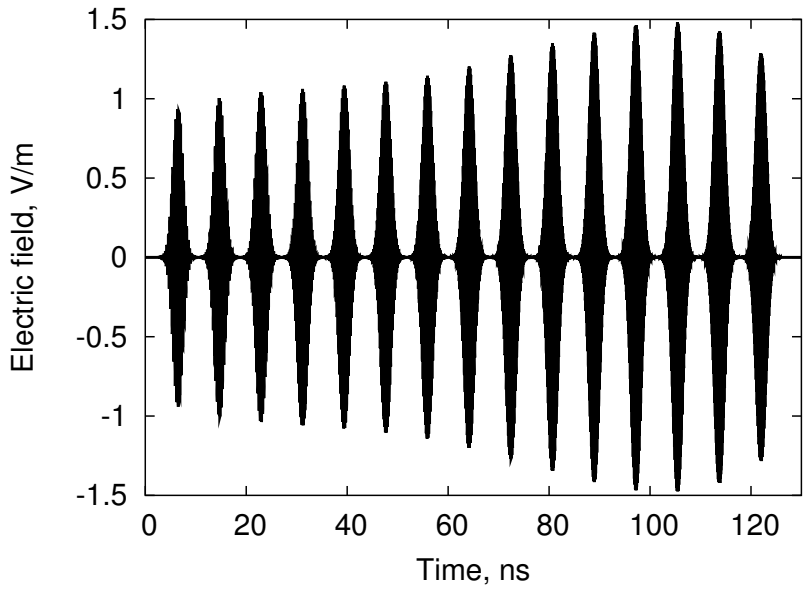

(a) $\theta = 90°, \phi = 0°$

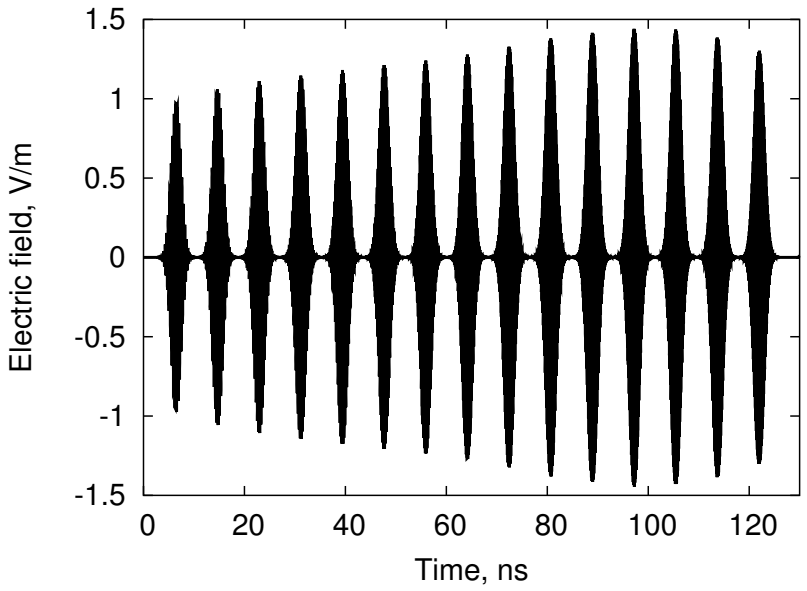

(b) $\theta = 90°, \phi = 60°$

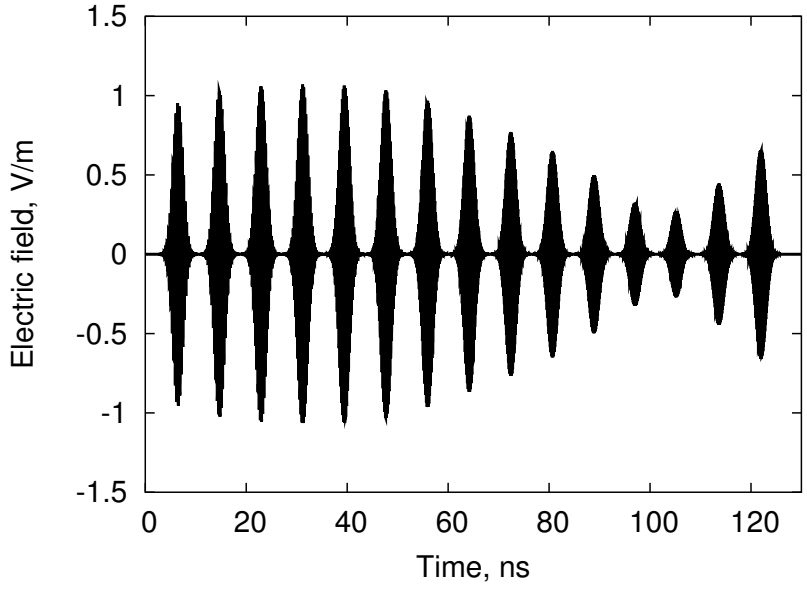

(c) $\theta = 90°, \phi = 120°$

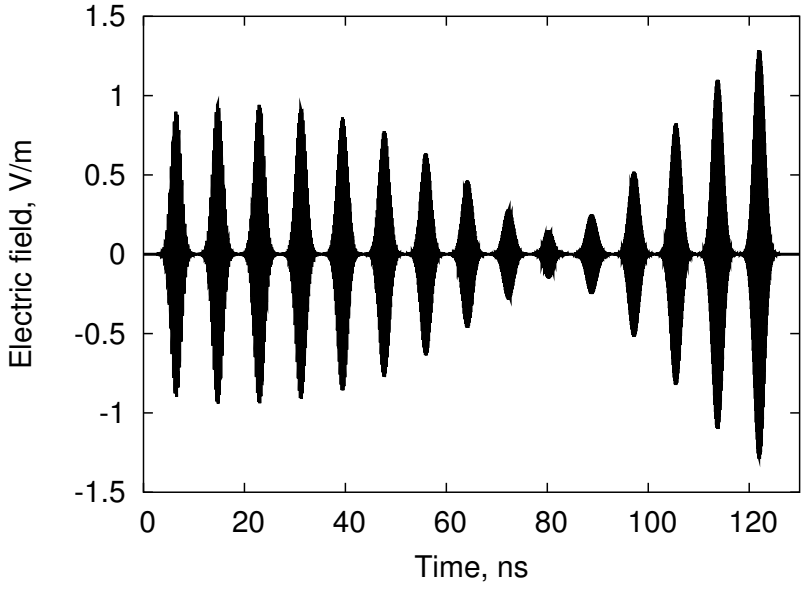

(d) $\theta = 90°, \phi = 180°$

Figure 18: Radiated pulses of Ant. C in a multi-band scheme

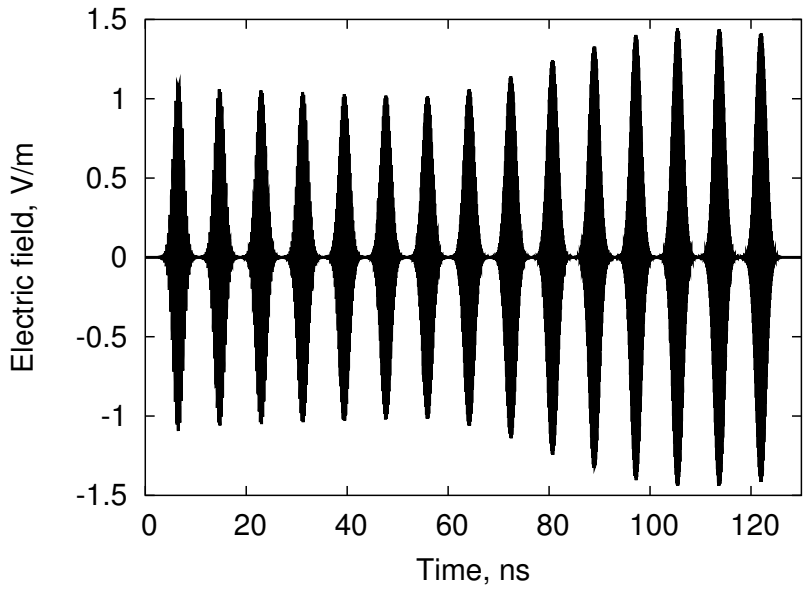

(a) $\theta = 90°, \phi = 0°$

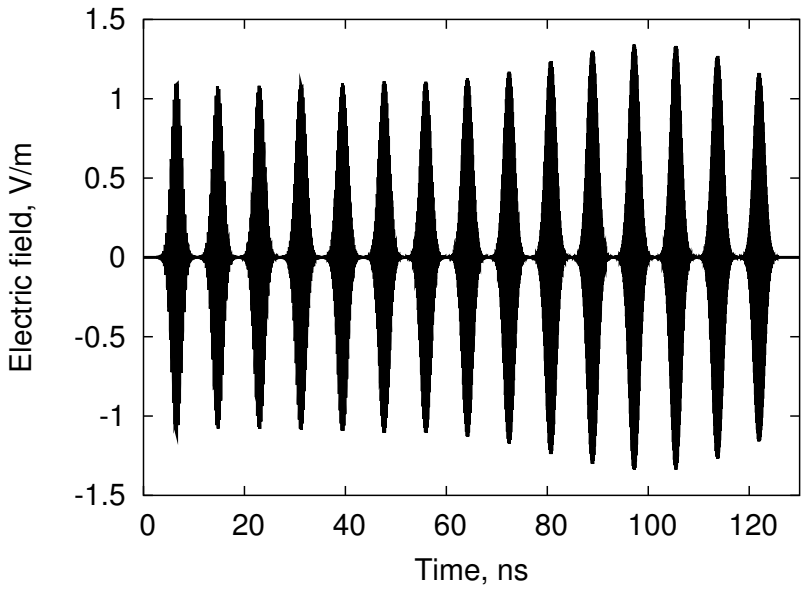

(b) $\theta = 90°, \phi = 60°$

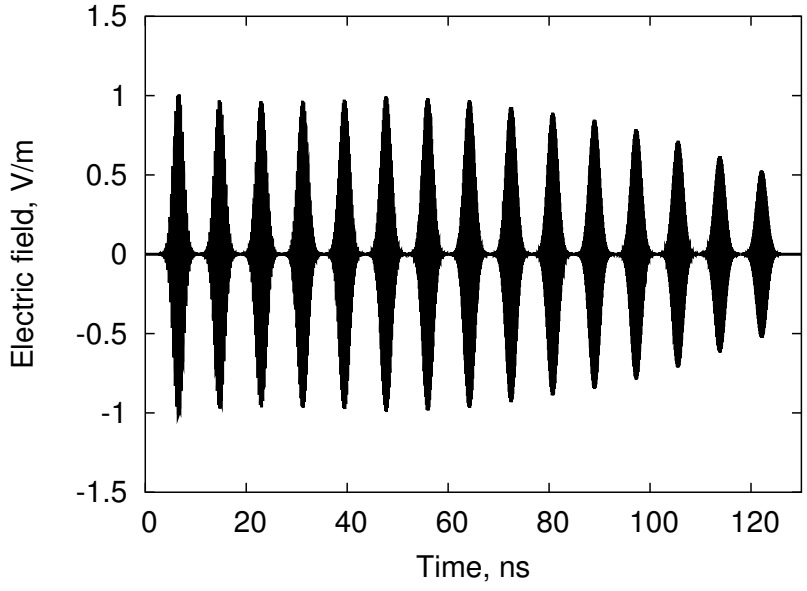

(c) $\theta = 90°, \phi = 120°$

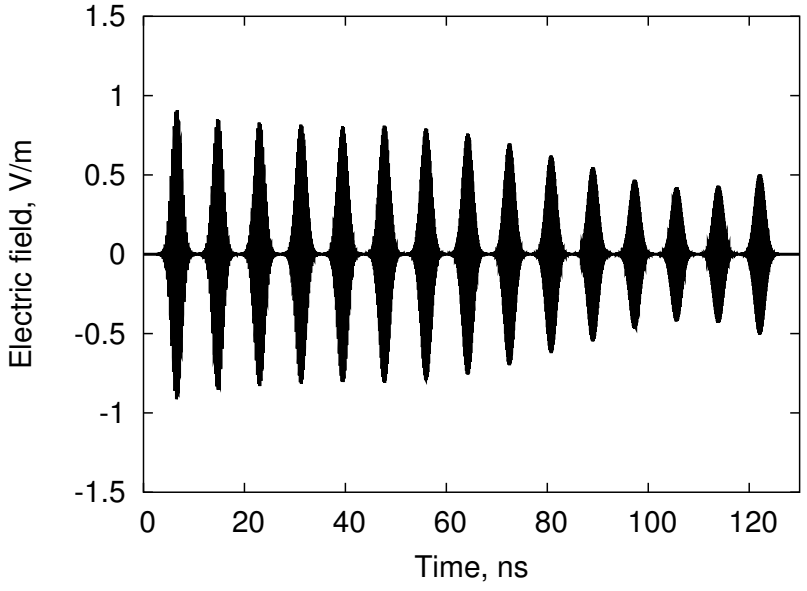

(d) $\theta = 90°, \phi = 180°$

Figure 19: Radiated pulses of Ant. D in a multi-band scheme